D. J. Xiao,E. D. Bloch,J. A. Mason,W. L. Queen,M. R. Hudson,N. Planas,J. Borycz,A. L. Dzubak,P. Verma,K. Lee,F. Bonino,V. Crocella,J. Yano,S. Bordiga,D. G. Truhlar,L. Gagliardi,C. M. Brown,J. R. Long

Oxidation of ethane to ethanol by N2O in a metal-organic framework with coordinatively unsaturated iron(II) sites
NATURE CHEMISTRY (2014) 6
DOI: 10.1038/NCHEM.1956

Oxidation of ethane to ethanol by nitrous oxide in a metal–organic framework with coordinatively-unsaturated iron(II) sites

Dianne J. Xiao[1], Eric D. Bloch[1], Jarad A. Mason[1], Wendy L. Queen[2], Matthew R. Hudson[3], Nora Planas[4], Joshua Borycz[4], Allison L. Dzubak[4], Pragya Verma[4], Kyuho Lee[2], Francesca Bonino[5], Valentina Crocellà[5], Junko Yano[6], Silvia Bordiga[5], Donald G. Truhlar[4], Laura Gagliardi[4], Craig M. Brown[3,7], Jeffrey R. Long[1,8]

Abstract

Enzymatic heme and non-heme high-valent iron-oxo species are known to activate strong C–H bonds with relative ease, yet duplicating this reactivity in a synthetic system remains a formidable challenge. While the instability of the terminal iron-oxo moiety is perhaps the foremost obstacle, steric and electronic factors also limit the activity of previously reported mononuclear iron(IV)-oxo compounds. In particular, while nature's non-heme iron(IV)-oxos possess high-spin $S = 2$ ground states, this electronic configuration has proven difficult to achieve in a molecular species. These challenges may be mitigated within metal-organic frameworks featuring site-isolated iron centers in a constrained, weak-field ligand environment. Here, we show that the metal-organic framework Fe_2(dobdc) and its magnesium-diluted analogue, $Fe_{0.1}Mg_{1.9}$(dobdc), are able to convert ethane into ethanol and acetaldehyde using nitrous oxide as the terminal oxidant. Electronic structure calculations indicate that the active oxidant is likely a high-spin $S = 2$ iron(IV)-oxo species.

---

[1] Department of Chemistry, University of California, Berkeley, California 94720-1460, USA
[2] The Molecular Foundry, Lawrence Berkeley National Laboratory, Berkeley, California 94720-1460, USA
[3] Center for Neutron Research, National Institute of Standards and Technology, Gaithersburg, Maryland 20899, USA
[4] Department of Chemistry, Chemical Theory Center, and Supercomputing Institute, University of Minnesota, Minneapolis, Minnesota, 55455-0431, USA
[5] Department of Chemistry, NIS and INSTM Reference Centres University of Turin, Via Quarello 15, I-10135 Torino, Italy
[6] Physical Biosciences Division, Lawrence Berkeley National Laboratory, Berkeley, California 94720-1460, USA
[7] Department of Chemical Engineering, University of Delaware, Newark, Delaware 19716, USA
[8] Materials Sciences Division, Lawrence Berkeley National Laboratory, Berkeley, California 94720, USA

Introduction

The selective and efficient conversion of light alkanes into value-added chemicals remains an outstanding challenge with tremendous economic and environmental impact,[1,2] especially considering the recent worldwide increase in natural gas reserves.[3] In nature, C–H functionalization is carried out by copper and iron metalloenzymes, which activate dioxygen and, through metal-oxo intermediates, facilitate two- or four-electron oxidations of organic substrates.[4,5,6,7] Duplicating this impressive reactivity in synthetic systems has been the focus of intense research. In particular, iron(IV)-oxo complexes have now been structurally characterized in various geometries (octahedral, trigonal bipyramidal) and spin states ($S = 1$, $S = 2$), and have proven to be competent catalysts for a variety of oxygenation reactions.[8,9] However, in the absence of a protective protein superstructure, terminal iron-oxo species are highly susceptible to a variety of decomposition pathways, including dimerization to form oxo-bridged diiron complexes, intramolecular ligand oxidation, and solvent oxidation.[10] Tethering a molecular iron species to a porous solid support such as silica or polystyrene could potentially prevent many of these side-reactions. In practice, however, complexes heterogenized in this manner are challenging to characterize by available techniques, and additional problems associated with steric crowding, site inaccessibility, and metal leaching inevitably arise.[11,12] Iron cations can also be incorporated into zeolites, either as part of the framework or at extraframework sites, producing reactive iron centers that have no direct molecular analogue. Fe-ZSM-5, for example, has been shown to oxidize methane to methanol stoichiometrically when pretreated with nitrous oxide.[13] However,

characterization of these materials is nontrivial due to the presence of multiple iron species, and the nature of the active sites in Fe-ZSM-5 remains largely a matter of speculation.[14]

The use of a metal-organic framework to support isolated terminal iron-oxo moieties is a currently unexplored yet highly promising area of research. The high surface area, permanent porosity, chemical and thermal stability, and synthetic tunability displayed by many of these materials makes them appealing in this regard. Additionally, metal-organic frameworks are typically highly crystalline with well-defined metal centers suited for characterization by single crystal and/or powder diffraction techniques. Furthermore, while molecular iron(IV)-oxo complexes generally utilize nitrogen-based chelating ligands, the metal cations in metal-organic frameworks are often ligated by weaker-field ligands, such as carboxylates and aryloxides, which are constrained in their coordination position by the extended framework structure. Thus, in addition to increased stability, terminal oxos in these materials might also have novel electronic properties and reactivity imparted by their unique coordination environment.

Herein, we show that the high-spin iron(II) centers within Fe_2(dobdc) (dobdc^{4-} = 2,5-dioxido-1,4-benzenedicarboxylate) can activate N_2O, most likely forming a transient, high-spin iron(IV)-oxo intermediate, which rapidly reacts to afford $Fe_2(OH)_2$(dobdc). Significantly, the magnesium-diluted analogue, $Fe_{0.1}Mg_{1.9}$(dobdc), is found to selectively oxidize ethane to ethanol in the presence of N_2O under mild conditions.

Results and Discussion

Of the three-dimensional iron(II)-containing metal-organic frameworks shown to be stable to desolvation,[15,16,17,18] few possess coordinatively-unsaturated metal centers in a single, well-defined environment. The compound Fe_2(dobdc) (**1**), also known as Fe-MOF-74 or CPO-27-Fe, is rare in this regard, as the hexagonal channels of the framework are lined with a single type of square pyramidal iron(II) site (see Figure 1a). The high density and redox-active nature of these open metal sites engender excellent O_2/N_2 and hydrocarbon separation properties.[18,19] However, with respect to the reactivity of the framework, only the hydroxylation of benzene to phenol and the oxidation of methanol to formaldehyde have been reported.[20,21] Thus, we embarked on a study of its reactivity towards nitrous oxide, a gaseous two-electron oxidant and O-atom transfer agent that is widely employed in industry, anticipating the generation of a highly reactive iron(IV)-oxo species capable of oxidizing strong C–H bonds.

We first investigated the binding of nitrous oxide to **1** under conditions in which the Fe–N_2O interaction is reversible. Experimental studies on the coordination chemistry of N_2O are scarce, as metal–N_2O adducts are challenging to synthesize due to the poor σ-donating and π-accepting properties of the molecule.[22] Indeed, of the several proposed binding modes, only one—end-on, η^1-N—has been structurally characterized in a molecular complex.[23] To establish the coordination mode of N_2O in **1**, powder neutron diffraction data, which are very sensitive to the atomic assignment of O and N, were collected on a sample dosed with various loadings of N_2O. At low loadings, the best fit was an average of approximately 60% η^1-O and 40% η^1-N coordination, with Fe–N_2O distances of 2.42(3) and 2.39(3) Å, respectively. In both cases, a bent Fe–N_2O angle close

to 120° is observed (see Figure 1b). Density functional theory (DFT) studies of N_2O-bound **1** using the M06 functional[24] show excellent agreement with experiment (see Figure S20). Furthermore, these calculations predict the η^1-O coordination mode to be favored over the η^1-N mode by just 1.1 kJ/mol (see Tables S17 and S22). This is consistent with the nearly equal population split observed, although the magnitude of the difference is smaller than the reliability of the calculations.

While η^1-O coordination with a bent Fe–O–N angle has been proposed in a variety of systems ranging from isolated metal atoms to iron zeolites,[22,25,26] η^1-N coordination with a bent Fe–N–N angle is much more unusual. It suggests little π-back-bonding from the metal d-orbitals into the π* of N_2O, in contrast to previously reported vanadium and ruthenium–N_2O adducts, which have linear metal–N–N–O geometries and for which π-interactions have been invoked as significant contributors to the stability of the complexes.[23,27,28,29] The bent geometry, long Fe–N_2O bond length, and mixed N- and O-coordination indicate N_2O is bound only weakly to the iron(II) centers in the framework, a hypothesis corroborated by *in-situ* transmission-mode infrared spectroscopy. Spectra collected on a thin-film of **1** dosed at room temperature with N_2O display a maximum at 2226 cm^{-1}, which is very close to the fundamental ν(N–N) transition for unbound N_2O (2224 cm^{-1}), suggesting a physically adsorbed phase with little to no perturbation of the N_2O molecule (see Figure S1). As expected, this interaction is fully reversible, and the band completely disappears under applied vacuum. Consistent with these experimental results, DFT studies calculate binding energies of 45.6 and 44.5 kJ/mol for the η^1-O and η^1-N modes, respectively, with a natural bond order analysis[30] showing weak back-bonding in both configurations (see Table S23).

Upon heating the N_2O-dosed framework to 60 °C, the material undergoes a drastic color change from bright green to dark red-brown that is suggestive of oxidization. In addition, *in situ* infrared studies using CO as a probe molecule show that the open metal sites, which coordinate CO strongly, have been almost entirely consumed (see Figure S9). Characterization of the resulting product is consistent with the formulation $Fe_2(OH)_2(dobdc)$ (**2**), in which each iron center is in the +3 oxidation state and bound to a terminal hydroxide anion (see Figure 2a). Compound **2** is likely formed via a fleeting iron-oxo intermediate, which rapidly undergoes H-atom abstraction, although the source of the H-atom has not been determined. Mössbauer spectroscopy was used to probe the local environment of the iron centers in the oxidized material. The ^{57}Fe Mössbauer spectrum of **2** consists of a doublet characterized by an isomer shift (δ) of 0.40(2) mm/s and a quadrupole splitting ($|\Delta E_Q|$) of 0.96(1) mm/s (see Figure 2b). The isomer shift for the iron centers in **2** is similar to the parameters obtained for the peroxide-coordinated iron(III) centers in $Fe_2(O_2)(dobdc)$,[18] and is consistent with other high-spin heme and nonheme iron(III) species.[31,32,33] In addition, the infrared spectrum of **2** shows the appearance of two new bands as compared to the unoxidized framework, which we assign as Fe–OH (667 cm^{-1}) and O–H (3678 cm^{-1}) vibrations. These bands shift to 639 and 3668 cm^{-1}, respectively, when $N_2{}^{18}O$ is employed for the oxidation; the observed differences of 28 and 10 cm^{-1} are very close to the theoretical isotopic shifts of 27 and 12 cm^{-1} predicted by a simple harmonic oscillator model (see Figure 3a). Partial oxidation of the framework is achieved by heating at 35 °C for 12 h, leading to the formation of $Fe_2(OH)_{0.6}(dobdc)$ (**2′**), which has a similar infrared spectrum (though the bands associated with Fe–OH are less intense) and Mössbauer parameters (see Table S9).

The framework maintains both crystallinity and porosity after oxidation, with a Brunauer-Emmett-Teller (BET) surface area of 1013 m^2/g and a Langmuir surface area of 1171 m^2/g. Rietveld analysis of powder X-ray diffraction data collected at 100 K on **2** firmly establishes the presence of a new Fe–O bond, but does not reveal whether a hydrogen atom is present. However, the Fe–OH bond distance of 1.92(1) Å is consistent with the bond lengths of previously reported octahedral iron(III)-hydroxide complexes (1.84-1.93 Å) (see Figure 3b).[34] In addition, the *trans* $Fe–O_{axial}$ bond is slightly elongated ($Fe–O_{axial}$ = 2.20(1) Å; average $Fe–O_{equatorial}$ = 2.04(1) Å), with the iron center shifted slightly out of the plane of the four equatorial oxygen atoms by 0.23(1) Å. EXAFS analysis of the same sample, as well as periodic DFT calculations, provide bond lengths that are consistent with those obtained from the diffraction data (see Table S8).

Surprisingly, the iron(III)-hydroxide species is capable of activating weak C–H bonds. When the partially oxidized sample **2′** is exposed to 1,4-cyclohexadiene (C–H bond dissociation energy of 305 kJ/mol)[35] at room temperature, benzene is produced as the sole product in quantitative yield. In the process, the framework converts entirely back to iron(II), as determined by Mössbauer spectroscopy. Such reactivity is rare but not unprecedented for iron(III)-hydroxide compounds. For instance, lipoxygenase, an enzyme that converts 1,4-dienes into alkyl hydroperoxides, is believed to proceed through a non-heme ferric hydroxide intermediate,[5] and several molecular lipoxygenase mimics have also been reported to activate the C–H bond of 1,4-cyclohexadiene and other 1,4-dienes.[36,37] However, the oxidizing power of **2** and **2′** is limited, and no reaction is observed with less activated C–H bonds.

Because the isolation of an iron(III)-hydroxide product from a reaction employing a two-electron oxidant strongly suggests the intermediacy of an iron(IV)-oxo species, we next carried out the oxidation in the presence of a hydrocarbon substrate containing stronger C–H bonds, specifically ethane (C–H bond dissociation energy of 423 kJ/mol), hoping to intercept the oxo species before its decay. Indeed, flowing an N_2O:ethane:Ar mixture (10:25:65) over the framework at 75 °C led to the formation of various ethane-derived oxygenates, including ethanol, acetaldehyde, diethyl ether, and other ether oligomers, as determined by ^{1}H NMR spectroscopy of the extracted products. The formation of ether products is not unprecedented, as N_2O-treated Fe-ZSM-5 forms a small amount of dimethylether in addition to methanol when exposed to methane, via a mechanism proposed to involve methyl radicals as well as multiple iron sites.[38] We hypothesized that the complex mixture of products was related to the close proximity of reactive iron centers, which are 8.75(2) Å and 6.84(1) Å apart across and along a channel, respectively, in **1**. To avoid oligomerization and over-oxidation, a mixed-metal metal-organic framework, $Fe_{0.1}Mg_{1.9}$(dobdc) (**3**), in which the iron(II) sites are diluted with redox-inactive magnesium(II) centers, was synthesized. The BET surface area of 1670 m^2/g for this material falls between the surface areas of the pure iron and pure magnesium frameworks (1360 and 1800 m^2/g, respectively). While determining the exact distribution of metal centers in heterometallic metal-organic frameworks is challenging, the unit cell parameters of **3** are also in between those of Fe_2(dobdc) and Mg_2(dobdc) (see Table S10), suggesting the formation of a solid solution rather than a mixture of two separate phases. Additionally, the Mössbauer spectrum of **3** shows sharp doublets with a significantly different quadrupole splitting than the all-iron analogue (2.25(1) mm/s versus 2.02(1)

mm/s in Fe_2(dobdc); see Table S9), indicating that the iron centers in the magnesium-diluted framework are in an altered, but uniform, environment. Thus, **3** is likely best described as containing either isolated iron centers or short multiiron segments dispersed evenly throughout a magnesium-based framework.

Exposure of **3** to N_2O and ethane under the same flow-through conditions yields the exclusive formation of ethanol and acetaldehyde in a 10:1 ratio, albeit in low yield (60% with respect to iron). Gas chromatography analysis of the headspace reveals no ethanol, acetaldehyde, or CO, suggesting the products remain bound to the framework (either at open iron or open magnesium sites), which likely explains the high ethanol selectivity. While the framework is still highly crystalline after N_2O/ethane treatment, Mössbauer spectroscopy reveals that roughly 90% of the iron centers have decayed into a species with similar spectral parameters as **2** (see Figure S18 and Table S9). We propose that formation of iron(III)-hydroxide or alkoxide decay products prematurely halts the catalytic cycle, which leads to substoichiometric yields of hydroxylated product (see Figure 4). Because glass can be a source of H-atoms, the reaction was subsequently repeated in a batch, rather than flow-through mode, in a Teflon-lined stainless-steel bomb, which produced both higher yields with respect to iron (turnover number = 1.6) and selectivities (25:1 ethanol:acetaldehyde), showing that the system can indeed be modestly catalytic if competing substrates are excluded. However, the yield based on ethane (roughly 1%) is still too low for practical purposes.

As the high reactivity of the iron-oxo species precluded isolation in both Fe_2(dobdc) and its magnesium-diluted analog, electronic structure calculations were performed on $Fe_2(O)_2$(dobdc) (**4**) to gain insight into the geometric and electronic

structure of iron-oxo units supported within the framework. First, periodic PBE+U[39,40] geometry optimizations were performed on **4** for the singlet, triplet, and quintet spin states. A quintet ground state was predicted, with a short Fe–O bond length of 1.64 Å, consistent with that of previously reported iron(IV)-oxo complexes (see Figure 5 and Table S11).[8] The periodic structure was then truncated to an 89-atom model cluster[41,42] containing three metal centers, six organic linkers, and an oxo moiety to facilitate calculations using more accurate methods. The cluster calculations were simplified by replacing the two peripheral iron(II) centers with closed-shell zinc(II) centers, which have the same charge and a similar ionic radius to iron(II) and magnesium(II) cations (see Figure S19). The geometry of this cluster was then optimized for the ground state, with all atoms except for the central iron and its first coordination sphere frozen at the coordinates from the periodic PBE+U optimization. As shown in Table 1, the M06[24] calculations also predict a quintet ground state. Further calculations were performed with several other exchange-correlation functionals, and in each case the ground state was found to be a quintet (see Tables S11–S16). Note that similar results were obtained when the Zn(II) centers in the 89-atom cluster were replaced with Mg(II) centers (see Tables S20 and S21).

The electronic structure of the cluster model of **4** was further examined with single-point multiconfigurational complete active space (CASSCF) calculations followed by second-order perturbation theory (CASPT2).[43,44] Again, the ground state is predicted to be the quintet state (see Table 1 and Table S18). Both M06 and CASPT2 yield a spin density of ~3.7 on iron, consistent with four unpaired spins mainly localized on the metal (see Tables S13 and S19). Density functional and CASPT2 calculations were also

performed on the cluster model of **2**; all calculations led to a high-spin sextet ground state for the iron(III) center (see Tables S11–S16 and Table S18).

Table 1 | Calculated relative energies (kJ/mol) of the cluster model of 4.

S	M06	CASPT2
0	210.6	249.4
1	136.4	127.6
2	0.0	0.0

While spectroscopic and theoretical studies have long attributed the reactivity of non-heme enzymatic and synthetic iron(IV)-oxo complexes to a quintet spin state,[45] only a small handful of mononuclear high-spin iron(IV)-oxo species have been characterized,[46,47,48,49] with all but one exhibiting a trigonal bipyramidal coordination geometry.[50] In these systems, the oxo moiety is either extremely unstable—$[Fe(O)(H_2O)_5]^{2+}$, for example, has a half life of roughly 10 s—or inaccessible to substrates due to bulky ligand scaffolds, leading to sluggish reactivity. On the other hand, the Fe_2(dobdc) framework features sterically accessible, site-isolated metal centers entrenched in a weak-field ligand environment. Utilizing these two properties, it is possible not only to generate such a species, albeit fleetingly, but also to direct it towards the facile activation of one of the strongest C–H bonds known.

Concluding remarks

The foregoing results demonstrate through reactivity studies, detailed characterization of decay products, and theoretical calculations that the iron-based metal-organic frameworks Fe_2(dobdc) and $Fe_{0.1}Mg_{1.9}$(dobdc) are very likely capable of

supporting fleeting iron(IV)-oxo species possessing an unusual $S = 2$ spin state. With this, Fe_2(dobdc) has now been shown to stabilize iron-superoxo, peroxo, hydroxo, as well as oxo intermediates, highlighting the promise of metal-organic frameworks both as catalysts and as scaffolds for interrogating reactive metal species. Future work will focus on: (i) further exploring the reactivity of Fe_2(dobdc) and its expanded analogues with ethane and other hydrocarbon substrates, as well as continued efforts to isolate the iron-oxo species, (ii) the use of dioxygen as the terminal oxidant in such systems, and (iii) the design, synthesis, and reactivity of other metal-organic frameworks with coordinatively-unsaturated iron sites.

Methods Summary

Synthesis of $Fe_2(OH)_{0.6}$(dobdc) (2′) and $Fe_2(OH)_2$(dobdc) (2)

An evacuated Schlenk flask containing fully desolvated Fe_2(dobdc) (100 mg, 0.33 mmol) was placed under an atmosphere of 30% N_2O and 70% N_2. The flask was immersed in an oil bath, and the temperature was increased by 10 °C every 12 h, from 25 °C up to 60 °C, to obtain $Fe_2(OH)_2$(dobdc) as a dark red-brown solid. When the reaction was stopped after 12 h at 35 °C, the partially oxidized $Fe_2(OH)_{0.6}$(dobdc) (as determined by Mössbauer spectroscopy) was obtained. Anal. Calc. for $C_8H_4Fe_2O_8$: C, 28.28; H, 1.19. Found: C, 29.18; H, 1.16. IR (solid-ATR): 3679 (m), 1532 (s), 1450 (s), 1411 (s), 1361 (s), 1261 (s), 1154 (w), 1129 (w), 1077 (w), 909 (m), 889 (s), 818 (s), 807 (s), 667 (s), 630 (m), 594 (s), 507 (s).

Synthesis of $Fe_{0.1}Mg_{1.9}$(dobdc) (3)

In a 500-mL Schlenk flask, H_4(dobdc) (1.8 g, 8.8 mmol), $MgCl_2$ (1.5 g, 15 mmol), and $FeCl_2$ (0.84 g, 6.6 mmol) were dissolved in a mixture of 310 mL of DMF and 40 mL of methanol. The reaction was stirred vigorously at 120 °C for 16 h. The precipitate was filtered and stirred with 250 mL of fresh DMF at 120 °C for 3 h. Two more DMF washes at 120 °C were performed, after which the precipitate was filtered and soaked in methanol at 60 °C. The methanol exchanges were repeated until no DMF stretches were apparent in the infrared spectrum. The framework was fully desolvated under dynamic vacuum (<15 μbar) at 210 °C for 2 days to afford $Fe_{0.1}Mg_{1.9}$(dobdc) as a bright yellow-green solid (2.0 g, 8.2 mmol, 93% yield). The iron to magnesium ratio was determined by ICP-OES. Anal. Calc. for $C_8H_2Fe_{0.1}Mg_{1.9}O_6$: C, 39.08; H, 0.82. Found: C, 39.37; H, 0.43.

IR (solid-ATR): 1577 (s), 1484 (m), 1444 (s), 1429 (s), 1372 (s), 1236 (s), 1210 (s), 1123 (m), 911 (m), 892 (s), 828 (s), 820 (s), 631 (s), 584 (s), 492 (s).

Reactivity of Fe_2(dobdc) (1) and $Fe_{0.1}Mg_{1.9}$(dobdc) (3) with N_2O and C_2H_6

In a typical flow-through experiment, a mixture of gases (2 mL/min N_2O, 10 mL/min C_2H_6, and 8 mL/min Ar for a total flow 20 mL/min) was flowed over a packed bed of metal-organic framework (50 to 100 mg) contained within a glass column. The column was heated to 75 °C for 24 h, after which the products were extracted with CD_3CN (3 × 1 mL) and analyzed by ^{1}H NMR using 1,4-dichlorobenzene as an internal standard. While a cold bath maintained at –78 °C was installed downstream of the glass reactor in order to collect condensable organic products, at the temperatures tested all the products appeared to remain bound to the framework.

In a typical batch experiment, a Parr bomb was charged with N_2O (1.5 bar) and C_2H_6 (7.5 bar) and heated to 75 °C in a sand bath. After 24 h, the bomb was cooled and the products extracted with CD_3CN.

Electronic structure calculations

The structures of **2** and **4** were optimized using periodic boundary conditions and the PBE+U exchange-correlation functional. From each of these structures, we carved out a model cluster containing three iron centers along a single helical chain and six organic linkers. These clusters are analogous to the 88-atom cluster model of Fe_2(dobdc) employed previously.[41] The cluster models were further simplified by substituting the two peripheral iron(II) centers with zinc(II) centers, while keeping only the central iron(II) in the cluster. Constrained geometry optimizations were performed where only the central iron and the six oxygen atoms (plus the hydroxide hydrogen in compound **2**) of its first coordination sphere were allowed to relax. Single-point multiconfigurational complete active space (CASSCF) calculations followed by second-order perturbation theory (CASPT2) were performed at PBE-optimized (PBE/SDD(Fe,Zn),6-31G(d)(C, H, O)) geometries of the cluster models of **2** and **4.**

Acknowledgments

Synthesis, basic characterization experiments, and all of the theoretical work, were supported by the U.S. Department of Energy, Office of Basic Energy Sciences, Division of Chemical Sciences, Geosciences, and Biosciences under award DE-FG02-12ER16362. Reactivity studies were supported by the Laboratory Directed Research and Development Program of Lawrence Berkeley National Laboratory. Work at the Molecular Foundry was supported by the Office of Science, Office of Basic Energy Sciences, of the U.S. Department of Energy under Contract No. DE-AC02-05CH11231. XAS experiments were performed at the Advanced Light Source (BL 10.3.2), Berkeley, under Contract DE-

AC02-05CH11231. X-ray diffraction experiments were performed at the Advanced Photon Source at Argonne National Laboratory (17-BM-B). S.B., F.B. and V.C. acknowledge financial support to Ateneo Project 2011 ORTO11RRT5. We also thank NSF for providing graduate fellowship support (D. J. X. and J. A. M.). In addition, we are grateful for the support of E. D. B. through a Gerald K. Branch fellowship in chemistry, P.V. through a Phillips 66 Excellence Fellowship, and M. R. H. through the NIST/NRC Fellowship Program. We thank Sachin Chavan for help with the infrared spectroscopy experiments and fruitful discussion.

Author information

Department of Chemistry, University of California, Berkeley, California 94720-1460, USA
Dianne J. Xiao, Eric D. Bloch, Jarad A. Mason, Jeffrey R. Long

The Molecular Foundry, Lawrence Berkeley National Laboratory, Berkeley, California 94720-1460, USA
Wendy L. Queen, Kyuho Lee

Center for Neutron Research, National Institute of Standards and Technology, Gaithersburg, Maryland 20899, USA
Matthew R. Hudson, Craig M. Brown

Department of Chemistry, Chemical Theory Center, and Supercomputing Institute, University of Minnesota, Minneapolis, Minnesota 55455-0431, USA
Nora Planas, Joshua Borycz, Allison L. Dzubak, Pragya Verma, Donald G. Truhlar, Laura Gagliardi

Nanoporous Materials Genome Center, University of Minnesota, 207 Pleasant St. SE, Minneapolis, Minnesota, 55455-0431, USA
Nora Planas, Joshua Borycz, Allison L. Dzubak, Pragya Verma, Donald G. Truhlar, Laura Gagliardi

Department of Chemistry, NIS and INSTM Reference Centres University of Turin, Via Quarello 15, I-10135 Torino, Italy.
Francesca Bonino, Valentina Crocellà, Silvia Bordiga

Physical Biosciences Division, Lawrence Berkeley National Laboratory, Berkeley, California 94720-1460, USA
Junko Yano

Author Contributions

D. J. X., E. D. B., and J. R. L. planned and executed the synthesis, characterization, and reactivity studies. J. A. M., W. L. Q., M. R. H., and C. M. B. analyzed the powder neutron and X-ray diffraction data. N. P. and P. V. performed the cluster DFT calculations. J. B. and K. L. performed the periodic DFT calculations. A. L. D. performed the CASSCF/PT2 calculations. D. G. T. and L. G. conceived and managed the computational efforts. F. B., V. C., and S. B. carried out the *in situ* transmission FTIR studies, and J. Y. supervised EXAFS analysis. All authors participated in the preparation of the manuscript.

Additional information

Further characterization, experimental, and computational details are described in the supplementary material available online at www.nature.com/naturechemistry (Tables S1-S19 and Figures S1-S20). Crystallographic data for Fe_2(dobdc) loaded with 0.35, 0.6, and 1.25 equivalents of N_2O and $Fe_2(OH)_2$(dobdc) (data collected at 100 and 298 K) have been deposited in the Cambridge Structural Database as CCDC 977092-977096.

Competing financial interests

The authors declare no competing financial interests.

Corresponding author

Correspondence to Jeffrey R. Long

References

1. Arakawa, H., Aresta, M., Armor, J. N., Barteau, M. A., Beckman, E. J., Bell, A. T., Bercaw, J. E., Creutz, C., Dinjus, E., Dixon, D. A., Domen, K., DuBois, D. L., Eckert, J., Fujita, E., Gibson, D. H., Goddard, W. A., Goodman, D. W., Keller, J., Kubas, G. J., Kung, H. H., Lyons, J. E., Manzer, L. E., Marks, T. J., Morokuma, K., Nicholas, K. M., Periana, R., Que, L., Nielson-Rostrup, J., Sachtler, W. M. H., Schmidt, L. D., Sen, A., Somorjai, G. A., Stair, P. C., Stults, B. R. & Tumas, W. Catalysis research of relevance to carbon management: progress, challenges, and opportunities. *Chem. Rev.* **101**, 953-996 (2001).
2. Bergman, R. G. Organometallic chemistry: C–H activation. *Nature* **446**, 391-393 (2007).
3. International Energy Agency. World energy outlook 2011: Are we entering a golden age of gas? http://www.worldenergyoutlook.org/goldenageofgas (2011).
4. Himes, R. A. & Karlin, K. D. Copper–dioxygen complex mediated C–H bond oxygenation: relevance for particulate methane monooxygenase (pMMO). *Curr. Opin. Chem. Biol.* **13**, 119-131 (2009).
5. Costas, M., Mehn, M. P., Jensen, M. P. & Que, L., Jr. Dioxygen activation at mononuclear nonheme iron active sites: enzymes, models, and intermediates. *Chem. Rev.* **104**, 939-986 (2004).

6. Meunier, B., de Visser, S. P. & Shaik, S. Mechanism of oxidation reactions catalyzed by cytochrome P450 enzymes. *Chem. Rev.* **104**, 3947-3980 (2004).
7. Wallar, B. J. & Lipscomb, J. D. Dioxygen activation by enzymes containing binuclear non-heme iron clusters. *Chem. Rev.* **96**, 2625-2658 (1996).
8. Hohenberger, J., Ray, K. & Meyer, K. The biology and chemistry of high-valent iron–oxo and iron–nitrido complexes. *Nat. Commun.* **3**, 720 (2012).
9. Nam, W. High-valent iron(IV)-oxo complexes of heme and non-heme ligands in oxygenation reactions. *Acc. Chem. Res.* **40**, 522-531 (2007).
10. Que, L., Jr. The road to non-heme oxoferryls and beyond. *Acc. Chem. Res.* **40**, 493-500 (2007).
11. Watton, S. P., Taylor, C. M., Kloster, G. M. & Bowman, S. C. Coordination complexes in sol–gel silica materials. *Prog. Inorg. Chem.* **51**, 333-420 (2002).
12. Leadbeater, N. E. & Marco, M. Preparation of polymer-supported ligands and metal complexes for use in catalysis. *Chem. Rev.* **102**, 3217-3274 (2002).
13. Panov, G. I., Sobolev, V. I., Dubkov, K. A., Parmon, V. N., Ovanesyan, N. S., Shilov, A. E. & Shteinman, A. A. Iron complexes in zeolites as a new model of methane monooxygenase. *React. Kinet. Catal. Lett.* **61**, 251-258 (1997).
14. Zecchina, A., Rivallan, M., Berlier, G., Lamberti, C. & Richhiardi, G. Structure and nuclearity of active sites in Fe-zeolites: comparison with iron sites in enzymes and homogeneous catalysts. *Phys. Chem. Chem. Phys.* **9**, 3483-3499 (2007).
15. Yoon, J. W., Seo, Y.-K., Hwang, Y. K., Chang, J.-S., Leclrec, H., Wuttke, S., Bazin, P., Vimont, A., Daturi, M., Bloch, E., Llewellyn, P. L., Serre, C., Horcajada, P., Grenèche, J.-M., Rodregues, A. E. & Férey, G. Controlled reducibility of a metal-organic framework with coordinatively unsaturated sites for preferential gas sorption. *Angew. Chem. Int. Ed.* **49**, 5949-5952 (2010).
16. Ma, S., Yuan, D., Chang, J.-S., Zhou, H.-C. Investigation of gas adsorption performances and H_2 affinities of porous metal-organic frameworks with different entatic metal centers. *Inorg. Chem.* **48**, 5398-5402 (2009).
17. Sumida, K., Horike, S., Kaye, S. S., Herm, Z. R., Queen, W. L., Brown, C. M., Grandjean, F., Long, G. J., Dailly, A. & Long, J. R. Hydrogen storage and carbon dioxide capture in an iron-based sodalite-type metal-organic framework (Fe–BTT) discovered *via* high-throughput methods. *Chem. Sci.* **1**, 184-191 (2010).
18. Bloch, E. D., Murray, L. J., Queen, W. L., Chavan, S., Maximoff, S. N., Bigi, J. P., Krishna, R., Peterson, V. K., Grandjean, F., Long, G. J., Smit, B., Bordiga, S., Brown, C. M. & Long, J. R. Selective Binding of O_2 over N_2 in a redox-active metal-organic framework with open iron(II) coordination sites. *J. Am. Chem. Soc.* **133**, 14814-14822 (2011).
19. Bloch, E. D., Queen, W. L., Krishna, R., Zadrozny, J. M., Brown, C. M. & Long, J. R. Hydrocarbon separations in a metal-organic framework with open iron(II) coordination sites. *Science* **335**, 1606-1610 (2012).
20. Märcz, M., Johnsen, R. E., Dietzel, P. D. C. & Fjellvåg, H. The iron member of the CPO-27 coordination polymer series: synthesis, characterization, and intriguing redox properties. *Microporous and Mesoporous Mater.* **157**, 62-74 (2012).

21. Bhattacharjee, S., Choi, J.-S., Yang, S.-T., Choi, S. B., Kim, J. & Ahn, W.-S. Solvothermal synthesis of Fe-MOF-74 and its catalytic properties in phenol hydroxylation. *J. Nanosci. Nanotechnol.* **10**, 135-141 (2010).
22. Tolman, W. B. Binding and activation of N_2O at transition-metal centers: recent mechanistic insights. *Angew. Chem. Int. Ed.* **49**, 1018-1024 (2010).
23. Piro, N. A., Lichterman, M. F., Harman, W. H. & Chang, C. J. A structurally characterized nitrous oxide complex of vanadium. *J. Am. Chem. Soc.* **133**, 2108-2111 (2011).
24. Zhao, Y. & Truhlar, D. G. The M06 suite of density functionals for main group thermochemistry, thermochemical kinetics, noncovalent interactions, excited states, and transition elements: two new functionals and systematic testing of four M06-class functionals and 12 other functionals. *Theor. Chem. Acc.* **120**, 215-241 (2008).
25. Delabie, A., Vinckier, C., Flock, M. & Pierloot, K. Evaluating the activation barriers for transition metal N_2O reactions. *J. Phys. Chem. A.* **105**, 5479-5485 (2001).
26. Heyden, A., Peters, B. & Bell, A. T. Comprehensive DFT study of nitrous oxide decomposition over Fe-ZSM-5. *J. Phys. Chem. B.* **109**, 1857-1873 (2005).
27. Bottomley, F. & Brooks, W. V. F. Mode of bonding of dinitrogen oxide (nitrous oxide) in (dinitrogenoxide)pentaammineruthenium. *Inorg. Chem.* **16**, 501-502 (1977).
28. Pamplin, C. B., Ma, E. S. F., Safari, N., Rettig, S. J. & James, B. R. The nitrous oxide complex, $RuCl_2(\eta^1\text{-}N_2O)(P\text{–}N)(PPh_3)$ (P–N = [*o*-(*N*,*N*-dimethylamino)phenyl]diphenylphosphine); low temperature conversion of N_2O to N_2 and O_2. *J. Am. Chem. Soc.* **123**, 8596-8597 (2001).
29. Paulat, F., Kuschel, T., Näther, C., Praneeth, V. K. K., Sander, O. & Lehnert, N. Spectroscopic properties and electronic structure of pentammineruthenium(II) dinitrogen oxide and corresponding nitrosyl complexes: binding mode of N_2O and reactivity. *Inorg. Chem.* **43**, 6979-6994 (2004).
30 Reed, A. E., Curtiss, L. A. & Weinhold, F. Intermolecular interactions from a natural bond orbital, donor-acceptor viewpoint. *Chem. Rev.* **88**, 899-926 (1998).
31. Macbeth, C. E., Golombek, A. P., Young, V. G., Jr., Yang, C., Kuczera, K., Hendrich, M. P., Borovik, A. S. O_2 activation by nonheme iron complexes: a monomeric Fe(III)–oxo complex derived from O_2. *Science* **289**, 938-941 (2000).
32. Dolphin, D. H., Sams, J. R., Tsin, T. B., Wong, K. L. Moessbauer-Zeeman spectra of some octaethylporphyrinato- and tetraphenylporphinatoiron(III) complexes. *J. Am. Chem. Soc.* **100**, 1711-1718 (1978).
33. Que, L., Jr. & True, A. E. Dinuclear iron- and manganese-oxo sites in biology. *Prog. Inorg. Chem.* **38**, 97-200 (1990).
34. Soo, H. S., Komor, A. C., Iavarone, A. T. & Chang, C. J. A hydrogen-bond facilitated cycle for oxygen reduction by an acid- and base-compatible iron platform. *Inorg. Chem.* **48**, 10024-10035 (2009).
35. Burkey, T. J., Majewski, M. & Griller, D. Heats of formation of radicals and molecules by a photoacoustic technique. *J. Am. Chem. Soc.* **108**, 2218-2221 (1986).
36. Goldsmith, C. R., Jonas, R. T. & Stack, T. D. P. C–H bond activation by a ferric methoxide complex: modeling the rate-determining step in the mechanism of lipoxygenase. *J. Am. Chem. Soc.* **124**, 83-96 (2002).

37. Goldsmith, C. R. & Stack, T. D. P. Hydrogen atom abstraction by a mononuclear ferric hydroxide complex: insights into the reactivity of lipoxygenase. *Inorg. Chem.* **45**, 6048-6055 (2006).
38. Starokon, E. V., Parfenov, M. V., Pirutko, L. V., Abornev, S. I., & Panov, G. I. Room-temperature oxidation of methane by α-oxygen and extraction of products from the FeZSM-5 surface. *J. Phys. Chem. C.* **115**, 2155-2161 (2011).
39. Perdew, J. P., Burke, K. & Ernzerhof, M. Generalized gradient approximation made simple. *Phys. Rev. Lett.* **77**, 3865-3868 (1996).
40. Franchini, C.; Kovácik, R.; Marsman, M.; Sathyanarayana Murthy, S.; He, J.; Ederer, C.; Kresse, G. Maximally localized Wannier functions in $LaMnO_3$ within PBE+U, hybrid functionals and partially self-consistent GW: an efficient route to construct ab initio tight-binding parameters for eg perovskites. *J. Phys. Condens. Mater.* **24**, 235602/1-17 (2012).
41. Verma, P., Xu, X., Truhlar, D. G. Adsorption on Fe-MOF-74 for C1-C3 hydrocarbon separation. *J. Phys. Chem. C.* ***117***, 12648-12660 (2013).
42. Maurice, R., Verma, P., Zadrozny, J. M., Luo, S., Borycz, J., Long, J. R., Truhlar, D. G. & Gagliardi, L. Single-ion magnetic anisotropy and isotropic magnetic couplings in the metal-organic framework Fe_2(dobdc). *Inorg. Chem.* **52**, 9379-9389 (2013).
43. Andersson, K., Malmqvist, P.-Å., Roos, B. O. Second order perturbation theory with a complete active space self-consistent field reference function. *J. Chem. Phys.* **96,** 1218-1226 (1992).
44 Andersson, K., Malmqvist, P. A., Roos, B. O., Sadlej, A. J., Wolinski, K. Second-order perturbation theory with a CASSCF reference function. *J. Phys. Chem.* **94**, 5483-5488 (1990).
45. Shaik, S., Hirao, H. & Kumar, D. Reactivity of high-valent iron–oxo species in enzymes and synthetic reagents: a tale of many states. *Acc. Chem. Res.* **40**, 532-542 (2007).
46. England, J., Guo, Y., Farquhar, E. R., Young, V. G., Jr., Münck, E., & Que, L., Jr. The crystal structure of a high-spin oxoiron(IV) complex and characterization of its self-decay pathway. *J. Am. Chem. Soc.* **132**, 8635-8644 (2010).
47. Lacy, D. C., Gupta, R., Stone, K. L., Greaves, J., Ziller, J. W., Hendrich, M. P. & Borovik, A. S. Formation, structure, and EPR detection of a high spin Fe^{IV}–oxo species derived from either an Fe^{III}–oxo or Fe^{III}–OH complex. *J. Am. Chem. Soc.* **132**, 12188-12190 (2010).
48. England, J., Guo, Y., Heuvelen, K. M., Cranswick, M. A., Rohde, G. T., Bominaar, E. L., Münck, E. & Que, L., Jr. A more reactive trigonal-bipyramidal high-spin oxoiron(IV) complex with a cis-labile site. *J. Am. Chem. Soc.* **133**, 11880-11883 (2011).
49. Bigi, J. P., Harman, W. H., Lassalle-Kaiser, B., Robles, D. M., Stich, T. A., Yano, J., Britt, R. D. & Chang, C. J. A high-spin iron(IV)-oxo complex supported by a trigonal nonheme pyrrolide platform. *J. Am. Chem. Soc.* **134**, 1536-1542 (2012).
50. Pestovsky, O., Stoian, S., Bominaar, E. L., Shan, X., Münck, E., Que, L., Jr. & Bakac, A. Aqueous Fe^{IV}=O: spectroscopic identification and oxo-group exchange. *Angew. Chem. Int. Ed.* **44**, 6871-6874 (2005).

Table of contents image:

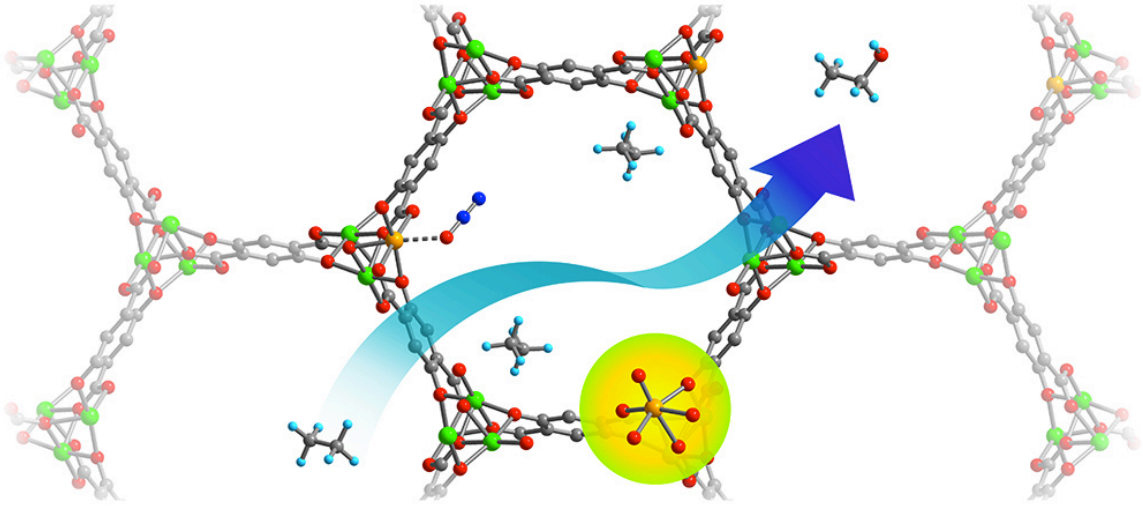

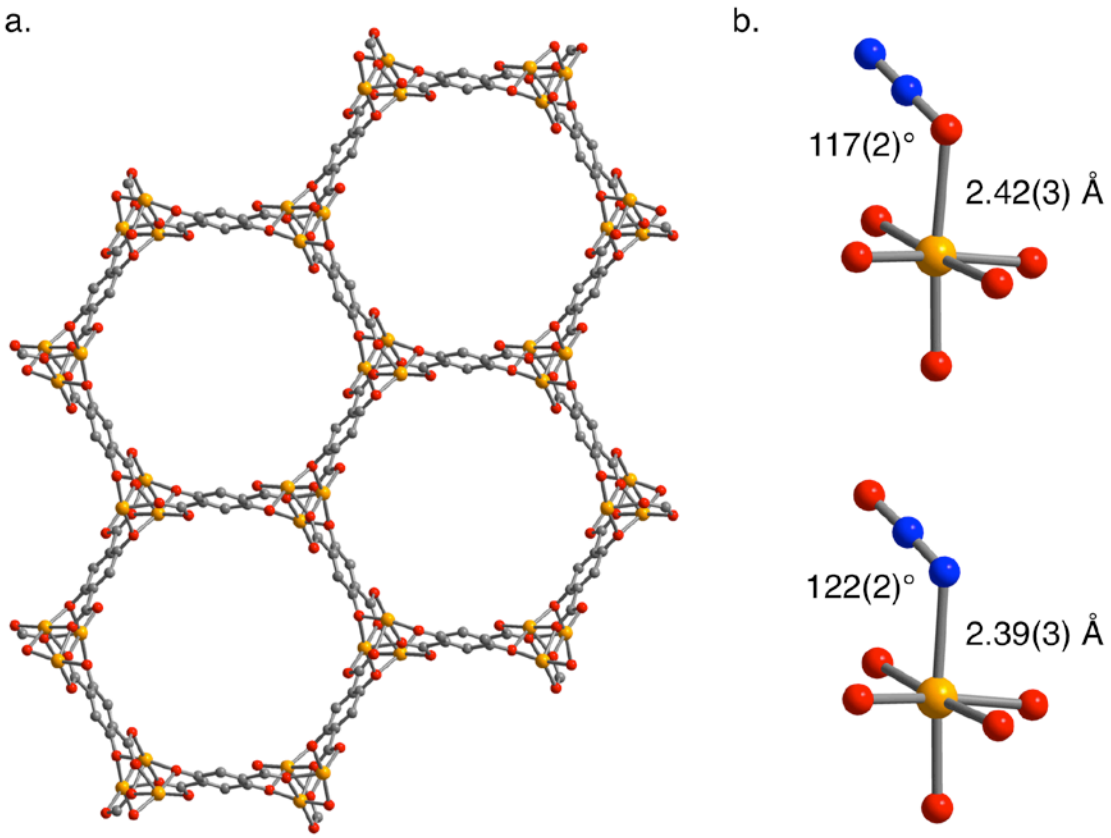

Figure 1 | Structure of bare and N_2O-dosed Fe_2(dobdc). a. Structure of Fe_2(dobdc), showing hexagonal channels lined with 5-coordinate iron(II) sites. The view is down the *c* axis, along the helical chains of iron(II) ions. **b.** Experimental structures for N_2O binding in Fe_2(dobdc) loaded with 0.35 equivalents of N_2O at room temperature and then slowly cooled to 10 K. The molecule binds with a bent Fe–N_2O angle, with a mixture of 60% η^1–O coordination and 40% η^1–N coordination. For comparison of calculated structures with experimental, see Figure S20.

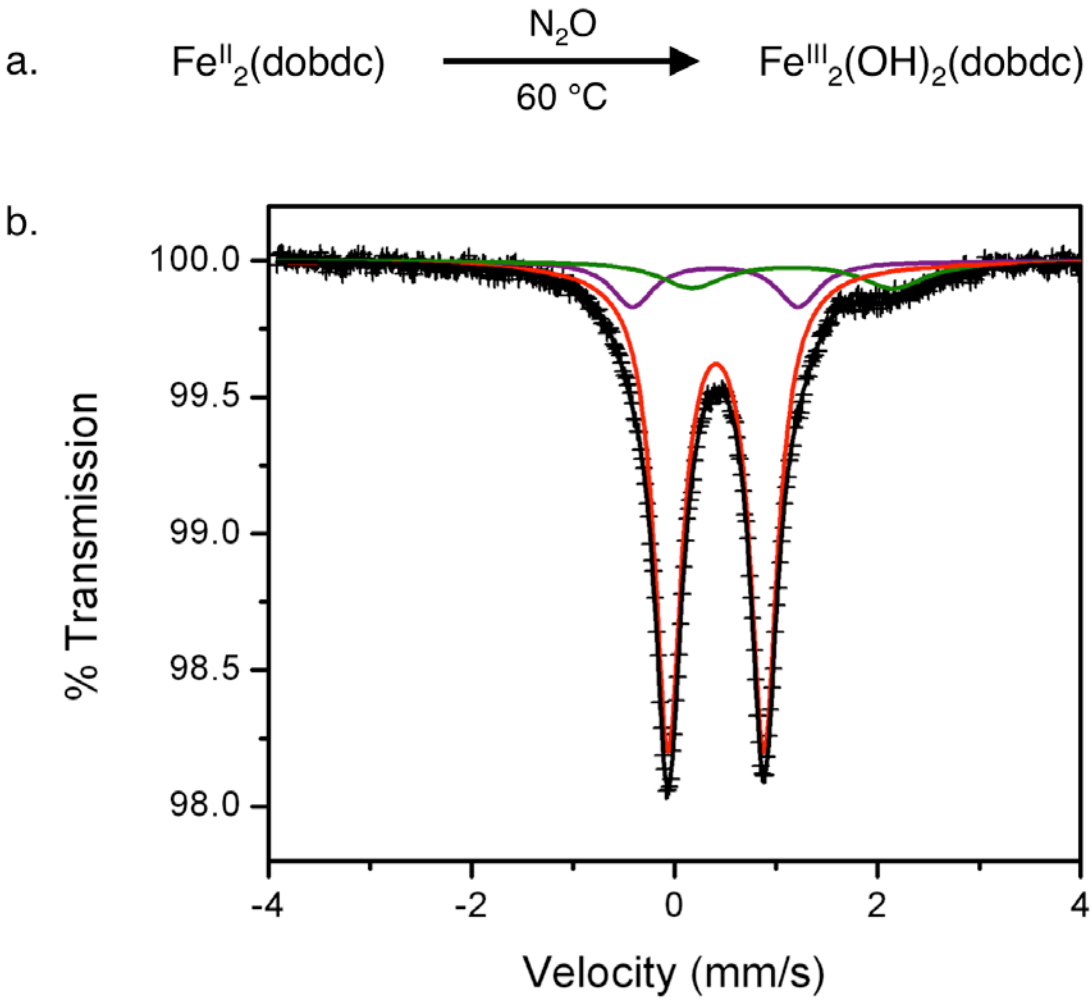

Figure 2 | Preparation and Mössbauer spectrum of $Fe_2(OH)_2(dobdc)$. a. Reaction scheme for the preparation of **2** from $Fe_2(dobdc)$. **b.** Mössbauer spectrum of **2**, with the fit in black. The red component has parameters consistent with high-spin Fe(III) (δ = 0.40(2) mm/s, $|\Delta E_Q|$, = 0.96(1) mm/s, area = 80(2)%). A minor component (green) is assigned as unreacted Fe(II) sites, and another minor component (purple) is assigned as an amorphous Fe(III) decomposition product.

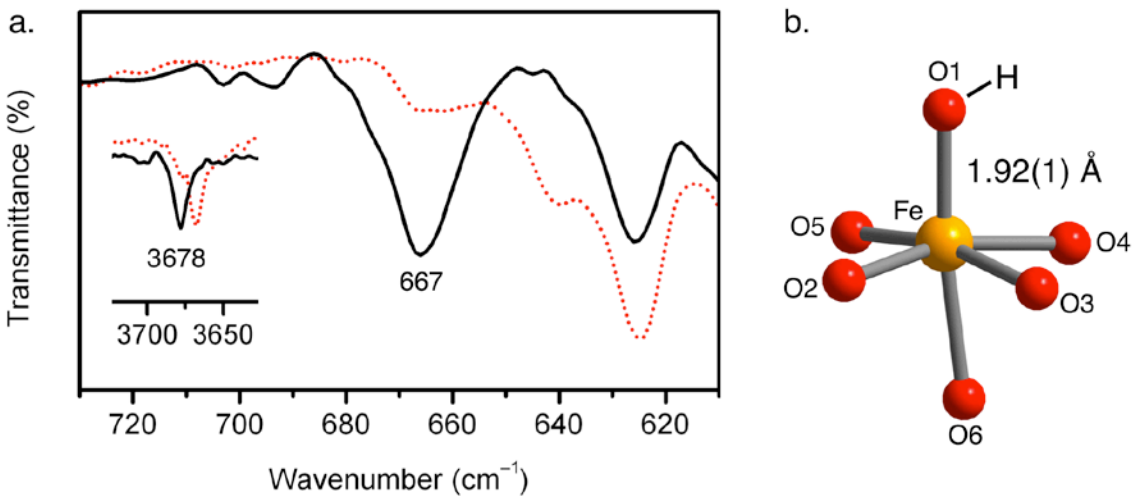

Figure 3 | Structure and infrared spectrum of $Fe_2(OH)_2(dobdc)$. a. Infrared spectrum of a partially oxidized sample, $Fe_2(OH)_{0.6}(dobdc)$ (black) and $Fe_2(^{18}OH)_{0.6}(dobdc)$ (dotted red). The peaks at 667 and 3678 cm^{-1} shift to 639 and 3668 cm^{-1}, respectively, upon ^{18}O labeling. **b.** The structure of $Fe_2(OH)_2(dobdc)$ obtained by powder X-ray diffraction data (100 K). Selected interatomic distances (Å) for **1**: Fe–O1 = 1.92(1); Fe–O2 = 2.01(1); Fe–O3 = 2.08(1); Fe–O4 = 2.04 (1); Fe–O5 = 2.04(1); Fe–O6 = 2.20(1); Fe–Fe = 3.16(1).

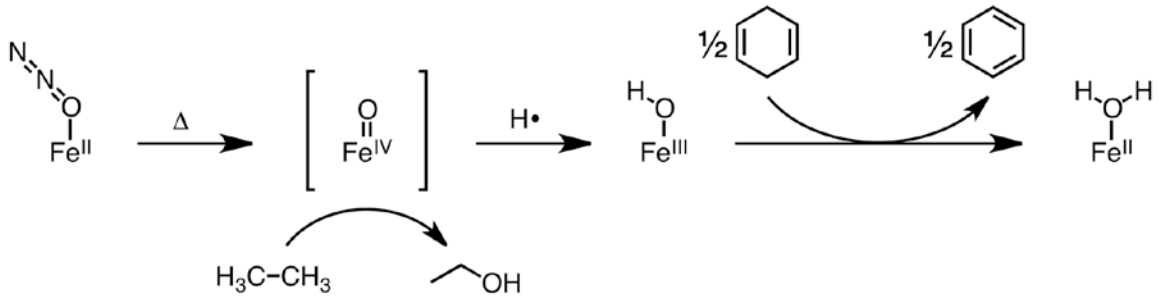

Figure 4 | N_2O activation and reactivity of Fe_2(dobdc).

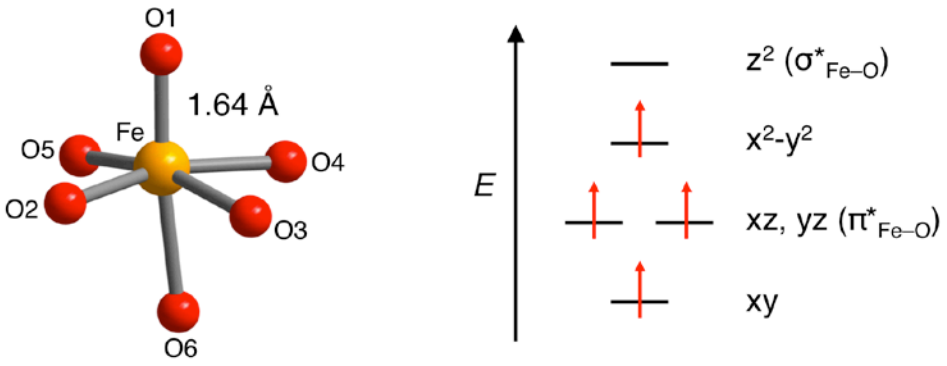

Figure 5 | Structure and qualitative MO diagram of $Fe_2(O)_2$(dobdc). DFT and CASSCF/PT2 studies predict a short iron-oxo bond (1.64 Å) and a high-spin, $S = 2$ spin ground state for iron(IV)-oxos installed in the Fe_2(dobdc) framework. Selected interatomic distances (Å) for **1**: Fe–O1 = 1.638; Fe–O2 = 2.004; Fe–O3 = 2.127; Fe–O4 = 2.019; Fe–O5 = 2.054; Fe–O6 = 2.140.

SUPPORTING INFORMATION

Oxidation of ethane to ethanol by nitrous oxide in a metal–organic framework with coordinatively-unsaturated iron(II) sites

Dianne J. Xiao[1], Eric D. Bloch[1], Jarad A. Mason[1], Wendy L. Queen[2], Matthew R. Hudson[3], Nora Planas[4], Joshua Borycz[4], Allison L. Dzubak[4], Pragya Verma[4], Kyuho Lee[2], Francesca Bonino[5], Valentina Crocellà[5], Junko Yano[6], Silvia Bordiga[5], Donald G. Truhlar[4], Laura Gagliardi[4], Craig M. Brown[3,7], Jeffrey R. Long[1,8]

Table of contents

[1] Department of Chemistry, University of California, Berkeley, California 94720-1460, USA
[2] The Molecular Foundry, Lawrence Berkeley National Laboratory, Berkeley, California 94720-1460, USA
[3] Center for Neutron Research, National Institute of Standards and Technology, Gaithersburg, Maryland 20899, USA
[4] Department of Chemistry, Chemical Theory Center, and Supercomputing Institute, University of Minnesota, Minneapolis, Minnesota, 55455-0431, USA
[5] Department of Chemistry, NIS and INSTM Reference Centres University of Turin, Via Quarello 15, I-10135 Torino, Italy
[6] Physical Biosciences Division, Lawrence Berkeley National Laboratory, Berkeley, California 94720-1460, USA
[7] Department of Chemical Engineering, University of Delaware, Newark, Delaware 19716, USA
[8] Materials Sciences Division, Lawrence Berkeley National Laboratory, Berkeley, California 94720, USA

1. Experimental

1.1. General

Unless otherwise noted, all procedures were performed under an N_2 atmosphere using standard glove box or Schlenk techniques. *N,N*-dimethylformamide (DMF) was dried using a commercial solvent purification system designed by JC Meyer Solvent Systems and then stored over 4 Å molecular sieves. Anhydrous methanol was purchased from commercial vendors, further dried over 3 Å sieves for 24 hours, and deoxygenated prior to being transferred to an inert atmosphere glove box, where it was stored over 3 Å molecular sieves. The ethane, argon, and nitrous oxide used in reactivity studies were purchased at 99.999%, 99.999%, and 99.998% purity, respectively. The 30% N_2O/N_2 mixture used to synthesize $Fe_2(OH)_2$(dobdc) was purchased from commercial vendors using 99.5% purity N_2O and 99.999% purity N_2. All other reagents were obtained from commercial vendors at reagent grade purity or higher and used without further purification.

Carbon, hydrogen, and nitrogen analyses were obtained from the Microanalytical Laboratory at the University of California, Berkeley. ^{1}H-NMR spectra were obtained using a Bruker AVB-400 instrument and peaks were referenced to residual solvent peaks.

1.2. Transmission and ATR Infrared Spectroscopy

Attenuated total reflectance infrared spectra were collected at 4 cm^{-1} resolution on a Perkin Elmer Avatar Spectrum 400 FTIR spectrometer equipped with a Pike attenuated total reflectance accessory. The instrument was placed inside an N_2-filled glove bag for measurement of air-sensitive samples.

In situ transmission FTIR spectra were collected at 2 cm^{-1} resolution on a Bruker Vertex 70 spectrophotometer equipped with a DTGS detector. The materials were examined in the form of self-supporting pellets (~15–20 mg/cm^2) mechanically protected with a pure gold frame. Samples were inserted in a homemade quartz IR cell, equipped with KBr windows and characterized by a very small optical path. The cell was attached to a conventional high vacuum glass line capable of a residual pressure less than 10^{-4} mbar. This setting allows both thermal treatment and adsorption–desorption cycles of molecular probes *in situ*. All materials were prepared and inserted into the IR cell inside an N_2-filled glove box to avoid contact with oxygen and moisture. Fe_2(dobdc) samples were activated under dynamic vacuum (residual pressure $<10^{-4}$ mbar) at 433 K for 18 h before being contacted with increasing pressures of N_2O (up to 40 mbar) (see Figure S1).

Contact with 40 mbar of N_2O causes the appearance of extremely strong bands in the 2280–2160 cm^{-1} spectral range, associated with ν(N–N) of N_2O, while the rest of the IR

spectrum is substantially unaffected. Dominant absorptions due to the framework modes below 1600 cm^{-1} does not allow the monitoring of the ν(N–O) band in N_2O, expected to be around 1286 cm^{-1}. The spectrum profile testifies the formation of a condensed phase inside the Fe_2(dobdc) channels, as the ν(N–N) does not present the expected profile of a free linear rotator (P and R branches with the lack of the pure vibrational transition, Q branch).

Figure S1b illustrates in detail the spectral range due to ν(N–N) band (spectra reported after background subtraction). The spectrum at highest coverage (blue curve) is characterized by a very intense band, ascribable to the ν(N–N) in N_2O molecule, behaving as an hindered rotator. The maximum is observed at 2226 cm^{-1}, a position very close to that expected for the fundamental transition of pure N_2O molecule (2224 cm^{-1}). The very small blue shift with respect to the position of N_2O gas allows us to assert that N_2O interacts weakly with the Fe(II) species, giving rise to a physically adsorbed (liquid-like) phase. The main peak is accompanied by further components at higher (clear maximum at 2240 cm^{-1}) and lower (broad features at 2220, 2214 and 2206 cm^{-1}) frequencies, suggesting that, at the measuring temperature (beam temperature), N_2O molecule still partially maintains its roto-vibrational profile (compare the spectra with that obtained in case of gaseous N_2O, blue dotted spectrum).

In case of Fe-silicalite the appearance of a doublet at 2282 cm^{-1} and at 2248 cm^{-1} was assigned to the formation of two slightly different Fe–N_2O adducts, while a component at 2226 cm^{-1} was associated to the formation of weaker adducts with Bronsted sites.[1] In the present case similar assignments are discarded, as all the above-mentioned signals disappear at the same rate upon outgassing at room temperature (see light grey spectra in Figure S1b). The total reversibility of these components further confirms the weak nature of the interaction of N_2O with the Fe(II) sites in Fe_2(dobdc) sample.

Prolonged heating in N_2O at 60 °C gives rise to a spectrum characterized by a strong band at 3678 cm^{-1} and by a clear component at 670 cm^{-1}. The peak at 3678 cm^{-1} can be associated to the ν(O–H) and the component at 670 cm^{-1} can be ascribed to the ν(Fe–OH). The formation of these hydroxide species is associated to the reactivity of N_2O, as testified by the intensity decrease of the band due to adsorbed N_2O (see inset (a) in Figure S8).

1.3. Mössbauer Spectroscopy

Iron-57 Mössbauer spectra were obtained at 295 K with a constant acceleration spectrometer and a cobalt-57 rhodium source. Prior to measurements the spectrometer was calibrated at 295 K with α-iron foil. Samples were prepared inside an N_2-filled glove box and contained 20 mg/cm^2 of sample (7 mg/cm^2 of iron) diluted with boron nitride.

All spectra were fit with symmetric Lorentzian quadrupole doublets using the WMOSS Mössbauer Spectral Analysis Software (www.wmoss.org).[2]

1.4. Low-Pressure Gas Adsorption Measurements

For all gas adsorption measurements, 100–200 mg of sample were transferred to a preweighed glass sample tube under an atmosphere of nitrogen and capped with a Transeal. Samples were then transferred to a Micromeritics ASAP 2020 gas adsorption analyzer and heated at a rate of 0.1 K/min from room temperature to a final temperature of 433 K and 483 K for Fe_2(dobdc) and $Fe_{0.1}Mg_{1.9}$(dobdc), respectively. Samples of $Fe_2(OH)_2$(dobdc) were degassed at room temperature. Samples were considered activated when the outgas rate at the degassing temperature was less than 2 μbar/min. Evacuated tubes containing degassed samples were then transferred to a balance and weighed to determine the mass of sample. The tube was transferred to the analysis port of the instrument where the outgas rate was again determined to be less than 2 μbar/min. Nitrogen gas adsorption isotherms at 77 K were measured in liquid nitrogen.

1.5. Powder Neutron Diffraction Data Collection and Refinement

Neutron powder diffraction (NPD) data (see Figures S2-S5) were collected on the high-resolution neutron powder diffractometer, BT1, at the National Institute of Standards and Technology (NIST) Center for Neutron Research. A 2.027 g activated sample of Fe_2(dobdc) was placed inside of a He-purged glove box and loaded into a vanadium sample can equipped with a gas loading lid. The sample was then sealed inside of the can using an indium o-ring and was then removed from the glove box and placed on a bottom-loading closed cycle refrigerator. The sample was first cooled to 10 K for data collection on the bare framework using a Ge(311) monochromator (λ = 2.0781 Å) and a 60 minute collimator. Fe_2(dobdc) was then warmed to room temperature where it was dosed with various predetermined amounts of N_2O gas, approximately 0.35, 0.60, and 1.25 N_2O molecules per Fe^{2+} site. For each gas dosing the pressure was first allowed to equilibrate over a ten minute period at room temperature, and then the sample was slowly cooled to 10 K over a period of approximately 2.5 hours for data collection. All NPD data were analyzed using the Rietveld method as implemented in EXPGUI/GSAS software package.[3] Fourier Difference Analysis of the bare Fe_2(dobdc) framework revealed no excess scattering density in the channel indicating that the sample was sufficiently activated. The structural model of the activated material was refined with all structural and peak profile parameters free to vary, resulting in a structure very similar to that previously determined (see Table S1).[4] Once completed, the same procedure was carried out for data obtained from the sample loaded with gas revealing both the site positions and orientations of framework bound N_2O (see Tables S2-S4).

Unlike X-rays, neutrons are scattered from the nucleus allowing neighboring atoms with similar electron densities to exhibit nonlinear variations in scattering power. Nitrogen and oxygen have coherent scattering lengths of 9.36 fm and 5.80 fm, respectively.[5] This implies that neutrons should be very sensitive to the atomic assignment of O and N, an especially important feature when considering the large esds associated with bond distances determined from position averaged powder data. Fourier Difference Analysis of the data obtained from the sample loaded with 0.35 N_2O per Fe^{2+} reveals that the N_2O binds in an end-on fashion with a distance of approximately 2.40(2) Å from the Fe^{2+} and is angled with respect to the framework surface at 118(2)° (see Figure S6). For assignment of the atoms responsible for binding to the metal site, we have tried both Fe^{2+}–O and Fe^{2+}–N binding. First, the occupancies of the N–N–O atoms were constrained to be equal. Once a stable refinement was achieved, the occupancies of the individual atoms in the N_2O molecule were allowed to vary independently of one another. In either case of M–O or M–N binding, the occupancies of both terminal N_2O atoms deviate significantly from the average value and lead to an improvement in the overall refinement. The observed increase and/or decrease in the occupancies correlate with our expectations based on the known differences in scattering lengths of the O and N and the results imply that pure O or N coordination at the metal site is incorrect. Further, the structural model shows only average distances for both N–N and N–O, around 1.15 Å, and so a clear assignment of the binding mechanism of the N_2O could not be made purely through assessment of bond distances. Considering all of these factors, we performed the refinement with mixed O and N binding of the N_2O molecules revealing an average of approximately 60% O and 40% N at the open metal site. The intramolecular N_2O angle was refined at a value of 178(2)°, which, within error of the neutron diffraction experiment, does not deviate from the expected linear geometry.

At higher loadings (0.6 and 1.25 equivalents of N_2O), disorder at the metal and the presence of multiple binding sites prevented accurate determination of the binding mode (see Figure S7). In particular, upon increasing the N_2O loading to 0.6 and then 1.25 N_2O per Fe^{2+}, there is further population of the site I molecule and then the subsequent introduction of a secondary adsorption site. Population of binding site II appears to induce a rearrangement of the site I molecule, referred to from this point forward as site Ia (see Figure S7). While the data is not good enough to distinguish the binding mechanism in these two different orientations, we can see a significant change in the angle of the N_2O with respect to the framework surface, which changes from ~120° to ~145°. Intermolecular distances between site I and II, on the order of 2.2 Å, are significantly shorter than the sum of the van der Waals radii for N (1.55 Å) and/or O (1.52 Å). As a result, this interaction is expected to be quite unfavorable. Further, the refined occupancies of site II, ~34%, and site I, ~68%, support the idea that the two sites are never simultaneously occupied.

1.6. Powder X-Ray Diffraction Data Collection and Refinement

X-ray diffraction data on $Fe_2(OH)_2(dobdc)$ were collected on Beamline 17-BM-B at the Advanced Photon Source at Argonne National Laboratory (see Figures S13-S14). The sample was first heated in the presence of N_2O, from room temperature to 60 °C over the course of two days. Excess N_2O was removed and the sample was pumped into an N_2 purged glove box where it was loaded into a 1.0 mm borosilicate capillary. The capillary was attached to a custom designed gas cell, to maintain an inert atmosphere, and then brought out of the glove box. The cell was then attached to an outgassing port on a Micromeritics ASAP 2020[**], where the remaining N_2 was removed and the sample was dosed with a small amount of He to serve as exchange gas. The capillary was then flame sealed for measurement. At 17-BM the capillary was mounted onto the goniometer head and then centered in the beam. Data was first collected at room temperature using a Si (111) monochromator (λ = 0.7291 Å, $\Delta E/E = 1.5*10^{-4}$) and then again after the sample was cooled at a rate of 2 K/min to 100 K in an N_2 cryostream. It should be noted that the sample was held at 100 K for 30 minutes prior to data measurement to allow for temperature equilibration. Rietveld analysis was carried out on both data sets in order to elucidate the site positions of the OH groups on the Fe^{3+} centers. Results of Rietveld analysis obtained from X-ray diffraction experiments of $Fe_2(OH)_2(dobdc)$ can be seen in Tables S5-S6.

For the unit cell determination of $Fe_xMg_{2-x}(dobdc)$, a microcrystalline sample of the material was gently ground and loaded into a 1.0 mm borosilicate capillary inside an N_2-filled glove box. The sample was sealed temporarily with silicone grease before it was taken out of the box and flame-sealed. Diffraction data were collected during an overnight scan in the 2θ range of 4–65° with 0.02° steps using a Bruker AXS D8 Advance diffractometer equipped with CuKα radiation (λ = 1.5418 Å), a Lynxeye linear position-sensitive detector, and mounting the following optics: Göbel mirror, fixed divergence slit (0.6 mm), receiving slit (3 mm), and secondary beam Soller slits (2.5°). The generator was set at 40 kV and 40 mA. A standard peak search, followed by indexing via the Single Value Decomposition approach,[6] as implemented in TOPAS-Academic,[7] allowed the determination of approximate unit cell dimensions. Precise unit cell dimensions were determined by performing a structureless Le Bail refinement in TOPAS-Academic.

1.7. EXAFS Data Collection and Refinement

X-ray absorption spectra (XAS) were collected at the Advanced Light Source (ALS) on beamline 10.3.2 with an electron energy of 1.9 GeV and an average current of 500 mA.

[**] Commercial materials and equipment are identified in this paper only to specify adequately the experimental procedure. In no case does such identification imply recommendation by NIST nor does it imply that the material or equipment identified is necessarily the best available for this purpose.

The radiation was monochromatized by a Si(111) double-crystal monochromator. Intensity of the incident X-ray was monitored by an N_2-filled ion chamber (I_0) in front of the sample. Fluorescence spectra were recorded using a seven-element Ge solid-state detector. The rising K-edge energy of Fe metal foil was calibrated at 7111.20 eV.

Data reduction of the XAS spectra was performed using custom-made software (Dr. Matthew Marcus). Pre-edge and post-edge contributions were subtracted from the XAS spectra, and the results were normalized with respect to the edge jump. Background removal in *k*-space was achieved through a five-domain cubic spline. Curve fitting was performed with Artemis and IFEFFIT software using ab initio-calculated phases and amplitudes from the program FEFF 8.2.[8,9]

1.8. Synthesis

Synthesis of $Fe_2(OH)_{0.6}$(dobdc) and $Fe_2(OH)_2$(dobdc)

Fe_2(dobdc) was synthesized according to previously reported procedures.[3a] An evacuated schlenk flask containing fully desolvated Fe_2(dobdc) (100 mg, 0.33 mmol) was placed under an atmosphere of 30% N_2O and 70% N_2. The flask was immersed in an oil bath, and the temperature was increased by 10 °C every 12 hours, from 25 °C up to 60 °C, to obtain $Fe_2(OH)_2$(dobdc) as a dark red-brown solid. If the reaction is stopped after 12 hours at 35 °C, the partially oxidized $Fe_2(OH)_{0.6}$(dobdc) (as determined by Mössbauer) is obtained. Anal. Calc. for $C_8H_4Fe_2O_8$: C, 28.28; H, 1.19. Found: C, 29.18; H, 1.16. IR (solid-ATR): 3679 (m), 1532 (s), 1450 (s), 1411 (s), 1361 (s), 1261 (s), 1154 (w), 1129 (w), 1077 (w), 909 (m), 889 (s), 818 (s), 807 (s), 667 (s), 630 (m), 594 (s), 507 (s).

Synthesis of $Fe_2(^{18}OH)_{0.6}$(dobdc)

Dried ^{18}O-labeled ammonium nitrate (50 mg, 0.58 mmol) was placed in a stainless steel reactor equipped with a two-way valve connected to a hose adapter. The reactor was evacuated and refilled with N_2 (3x) and then heated, closed, to 200 °C. After 24 hours, the reactor was cooled to 0 °C, and the evolved $N_2{}^{18}O$ was carefully condensed into an evacuated schlenk flask cooled to 77 K containing Fe_2(dobdc) (15 mg, 0.05 mmol). The sample was allowed to react for 12 hours at 35 °C, after which the partially oxidized sample was analyzed by IR.

Synthesis of $Fe_{0.1}Mg_{1.9}$(dobdc)

In a 500 mL schlenk flask, H_4(dobdc) (1.75 g, 8.8 mmol), $MgCl_2$ (1.47 g, 15.4 mmol), and $FeCl_2$ (0.84 g, 6.6 mmol) were dissolved in DMF (310 mL) and MeOH (40 mL). The reaction was stirred vigorously at 120 °C for 16 hours. The precipitate was filtered and stirred in fresh DMF (250 mL) at 120 °C for three hours. Two more DMF washes at 120 °C were performed, after which the precipitate was filtered and soaked in methanol at 60

°C. The methanol exchanges were repeated until no DMF stretches were visible by IR. The framework was fully desolvated under dynamic vacuum (<15 μbar) at 210 °C for 2 days to afford $Fe_{0.1}Mg_{1.9}$(dobdc) as a bright yellow-green solid (2.02 g, 8.2 mmol, 93% yield). $Fe_{0.44}Mg_{1.56}$(dobdc) and other analogs with different Fe:Mg ratios can be obtained by simply varying the ratio of $MgCl_2$ and $FeCl_2$ while keeping all other synthetic conditions the same. The iron to magnesium ratio was determined by ICP-OES. Anal. Calc. for $C_8H_2Fe_{0.1}Mg_{1.9}O_6$: C, 39.08; H, 0.82. Found: C, 39.37; H, 0.43. IR (solid-ATR): 1577 (s), 1484 (m), 1444 (s), 1429 (s), 1372 (s), 1236 (s), 1210 (s), 1123 (m), 911 (m), 892 (s), 828 (s), 820 (s), 631 (s), 584 (s), 492 (s).

1.9. Reactivity

Cyclohexadiene Reactivity of $Fe_2(OH)_{0.6}$(dobdc)

Neat cyclohexadiene (160 mg, 2.0 mmol) was added to $Fe_2(OH)_{0.6}$(dobdc) (66 mg, 0.125 mmol Fe^{III}, determined by Mössbauer) and allowed to react for 24 hours, during which a visible color change from red-brown to light yellow was observed. The sample was then extracted with CD_3CN (3 × 1 mL), and the products analyzed by ^1H NMR using 1,2,4,5-tetramethylbenzene as an internal standard. Benzene as the sole product was obtained in quantitative yield.

Reactivity of Fe_2(dobdc) and $Fe_{0.1}Mg_{1.9}$(dobdc) with N_2O and C_2H_6

In a typical flow-through experiment, a mixture of gases (2 mL/min N_2O, 10 mL/min C_2H_6, and 8 mL/min Ar for a total flow 20 mL/min) was flowed over a packed bed of metal–organic framework (50 to 100 mg) contained within a glass column. The column was heated to 75 °C for twenty-four hours, after which the products were extracted with CD_3CN (3 × 1 mL) and analyzed by ^1H NMR using 1,4-dichlorobenzene as an internal standard. While a cold bath maintained at –78 °C was installed downstream of the glass reactor in order to collect condensable organic products, at the temperatures tested all the products appear to remain bound to the framework. Yield for $Fe_{0.1}Mg_{1.9}$(dobdc): 9.5:1 ethanol:acetaldehyde, 60% yield based on Fe.

In a typical batch experiment, a Parr bomb was charged with 50-100 mg of $Fe_{0.1}Mg_{1.9}$(dobdc), N_2O (1.5 bar), and C_2H_6 (7.5 bar) and heated to 75 °C in a sand bath. After twenty-four hours, the bomb was cooled and the products extracted with CD_3CN. Yield for $Fe_{0.1}Mg_{1.9}$(dobdc): 25:1 ethanol:acetaldehyde, 1.6 turnovers based on Fe. In a typical experiment, this corresponds to functionalization of roughly 1% of the ethane molecules.

Control Experiments

No products were observed if N_2O, ethane, or Fe_2(dobdc)/$Fe_{0.1}Mg_{1.9}$(dobdc) was removed from the reaction mixture. The same flow-through and batch experiments performed on Mg_2(dobdc) led to no observed products. The same conditions applied to Fe_2(dobdc) diluted in Mg_2(dobdc) did not lead to a clean reaction (unlike $Fe_{0.1}Mg_{1.9}$(dobdc)). Finally, an autoxidation process was ruled out by repeating the batch experiment with added O_2 (1 bar), N_2O (1.5 bar), and C_2H_6 (7.5 bar). The yield was significantly lower (11% based on iron) and the ethanol selectivity much worse (1:2.67 ethanol:acetaldehyde), indicating that the reported reactivity is not due to autoxidation.

2. Computational

2.1. Periodic Systems

Starting from the experimental powder X-ray crystal structure, the periodic structures for **2** and **4** were fully optimized using periodic density functional theory as implemented in the *Vienna ab initio simulation package (VASP)*[10] employing the generalized gradient approximation exchange-correlation functional PBE.[11] A Hubbard *U* correction[12] of 5 eV was added to the intra-site Coulomb interactions of the d-orbitals of the iron atoms to decrease the delocalization of electron density that results from the presence of the self-interaction of electrons in the PBE non-hybrid density functional. The VASP calculations use projector-augmented wave potentials to describe the interaction between core and valence electrons. A plane-wave kinetic energy cutoff of 610 eV was used and the integration over the irreducible Brillouin zone was carried out over a 3×3×3 *k*-points grid. Atomic positions were relaxed until the forces were lower than 0.06 eV/A. All possible spin states were considered.

2.2. Cluster Calculations

From the initial periodic structures of **2** and **4**, we designed two corresponding model clusters containing three neighboring metal centers (along a single helical chain) and their first coordination spheres. These clusters are analogous to the recently reported[13] 88-atom cluster for Fe_2(dobdc), which contained three pentacoordinate Fe(II) centers and six organic linkers. As in the case of the 88-atom cluster model, the cluster model of **4** (containing 89 atoms, equivalent to the 88-atom cluster plus an additional O atom coordinated to the central Fe) and the cluster model of **2** (containing 90 atoms, equivalent to the 88-atom cluster plus an additional OH group coordinated to the central Fe) were designed to maintain an overall zero charge for the model system and to preserve a good representation of the first coordination sphere of the central iron atom from the periodic structure. We note that the charge of the cluster was set to zero by addition of protons. The cluster models were simplified by substituting the two peripheral Fe(II) ions with Zn(II) ions, while keeping only the central Fe ion in the cluster (note that we do not replace Fe(II) ions by Zn(II) ions for the periodic calculations).

Two-step constrained geometry optimizations were performed. In the first step, the protons added to neutralize the cluster charge were optimized, while all the other atoms were kept in fixed positions. In the second step, only the central Fe and its first coordination sphere were allowed to relax. The first coordination sphere consists of the Fe atom, the five O atoms of the bare MOF, and the atoms of the adsorbate (O, OH, or N_2O); since this involves optimizing six atoms of the bare MOF, it is denoted “opt6” in the notation of our previous work.[13] All the optimizations were followed by frequency

calculations to confirm that the stationary point was a minimum, which was indicated by the absence of any imaginary frequency in the optimized degrees of freedom.

All density functional cluster calculations used the *Gaussian 09* software package or a locally modified version of *Gaussian 09*.[14] The PBE,[11] M06-L,[15] M06,[16] M08-SO,[17] MPW1B95,[18] and PW6B95[19] exchange-correlation functionals were employed. For the Minnesota density functionals (M06-L, M06, M08-SO, MPW1B95, and PW6B95), an ultrafine grid (99 radial nodes and 590 angular nodes) was used to perform numerical integrations. The *stable=opt* keyword of *Gaussian* was used to test the stability of the Kohn-Sham Slater determinant and converge to a stable solution. An automatic density-fitting set generated by the *Gaussian* program was used to reduce the cost for calculations done with the local density functionals, PBE and M06-L. The 6-31G(d)[20] basis set was used for H, C, N, O, and Mg while the Stuttgart [8s7p6d1f | 6s5p3d1f] ECP10MDF contracted effective core potential basis set[21] was employed for Fe and Zn. Single-point calculations were performed with the 6-311+G(2df,p)[22] basis set for H, C, and O and the Stuttgart [8s7p6d1f | 6s5p3d1f] ECP10MDF contracted effective core potential basis set for Fe and Zn. These basis sets have been previously successfully employed in the study of molecular systems with similar M=O and M–OH motifs.[23]

2.3. Multireference Calculations

Single-point multiconfigurational complete active space[24] (CASSCF) calculations followed by second-order perturbation theory (CASPT2)[25] were performed at the DFT-optimized (PBE/SDD(Fe, Zn), 6-31G(d) (C, H, O)) geometries of the cluster models of **2** and **4**. These calculations were performed with the *Molcas 7.8* software package[26]. Scalar relativistic effects were included by use of the second order Douglas–Kroll–Hess Hamiltonian[27]. The computational cost arising from the two-electron integrals was reduced by employing the Cholesky decomposition technique (RICD).[28] The relativistic all-electron ANO-RCC basis sets[29] were used for all atoms; in particular, the ANO-RCC-VTZP basis set was used for Fe, for the five first-coordination-sphere O atoms of Fe in the MOF fragment, and for the O or OH atoms of the adsorbate. ANO-RCC-VDZP was used for the Zn and all other O atoms, and ANO-RCC-MB was used for all C and H atoms. No symmetry (point group C_1) was used, and all possible spin states were considered. The default IPEA shift of 0.25 eV was used in CASPT2, along with an imaginary shift of 0.2 eV.

An active space containing 10 electrons in 11 orbitals (10,11) was used for the cluster model of **4**. An active space containing 5 electrons in 5 orbitals (5,5), which contains the five d electrons of Fe(III) in the five 3d orbital was used for the cluster model of **2**. The sigma bonding orbital of the metal to the –OH ligand is doubly occupied in the inactive space, along with the five other Fe–O sigma bonding orbitals.

3. Supplemental Tables

Supplementary Table S1 | Rietveld Refinement (10 K) of Fe_2(dobdc). Fractional atomic coordinates, occupancies, and isotropic displacement parameters obtained from Rietveld refinement of structural model of the bare Fe_2(dobdc) framework at 10 K, space group R-3, a = 26.1826(6) Å, c = 6.8506(2) Å , and V = 4067.1(2) Å^3.

Atom	x	y	z	occ.	Uiso*100
Fe	0.3815(2)	0.3518(2)	0.1416(5)	1.0	0.4(1)
O1	0.3293(3)	0.2963(3)	0.369(1)	1.0	0.4(1)
O2	0.3001(3)	0.2259(3)	0.600(1)	1.0	0.4(1)
O3	0.3550(3)	0.2737(3)	0.011(1)	1.0	0.4(1)
C1	0.3189(3)	0.2453(3)	0.4267(9)	1.0	0.51(6)
C2	0.3278(3)	0.2063(3)	0.2915(8)	1.0	0.51(6)
C3	0.3441(3)	0.2221(3)	0.0908(8)	1.0	0.51(6)
C4	0.3490(3)	0.1809(3)	-0.030(1)	1.0	0.51(6)
H	0.3621(5)	0.1922(5)	-0.173(2)	1.0	1.8(3)

Supplementary Table S2 | Rietveld Refinement (10 K) of $Fe_2(dobdc)(N_2O)_{0.7}$. Fractional atomic coordinates, occupancies, and isotropic displacement parameters obtained from Rietveld refinement of structural model of the 0.35 N_2O per Fe^{2+} in the $Fe_2(dobdc)$ framework at 10 K, space group R-3, a = 26.1660(4) Å, c = 6.8595(2) Å , and V = 4067.2(2) $Å^3$.

Atom	x	y	z	occ.	Uiso*100
Fe	0.3819(1)	0.3520(2)	0.1437(4)	1.0	0.49(5)
O1	0.3279(2)	0.2957(2)	0.3676(8)	1.0	0.20(4)
O2	0.3010(2)	0.2272(2)	0.6019(7)	1.0	0.20(4)
O3	0.3550(2)	0.2738(2)	0.0084(8)	1.0	0.20(4)
C1	0.3193(2)	0.2463(2)	0.4292(7)	1.0	0.42(2)
C2	0.3275(2)	0.2063(2)	0.2887(7)	1.0	0.42(2)
C3	0.3438(2)	0.2213(2)	0.0924(7)	1.0	0.42(2)
C4	0.35061(2)	0.1817(2)	-0.0272(7)	1.0	0.42(2)
H	0.3619(4)	0.1930(3)	-0.1712(15)	1.0	1.3(2)
O11	0.471(1)	0.358(1)	0.272(4)	0.22(1)	1.6(8)
N12	0.5174(5)	0.3960(4)	0.2071(17)	0.371(7)	2.9(3)
N13	0.5607(6)	0.4314(6)	0.1533(26)	0.223(6)	1.6(4)
N11a	0.4718(9)	0.3605(9)	0.2628(32)	0.161(7)	1.1(6)
O13a	0.562(2)	0.433(2)	0.146(7)	0.16(1)	3(1)

Supplementary Table S3 | Rietveld Refinement (10 K) of $Fe_2(dobdc)(N_2O)_{1.2}$. Fractional atomic coordinates, occupancies, and isotropic displacement parameters obtained from Rietveld refinement of structural model of the 0.60 N_2O per Fe^{2+} in the $Fe_2(dobdc)$ framework at 10 K, space group R-3, a = 26.1577(4) Å, c = 6.8671(2) Å, and V = 4069.1(2) $Å^3$.

Atom	x	y	z	occ.	Uiso*100
Fe	0.3829(1)	0.3523(2)	0.1428(5)	1.0	0.94(5)
O1	0.3268(2)	0.2945(2)	0.3667(8)	1.0	0.17(4)
O2	0.3019(2)	0.2274(2)	0.6000(7)	1.0	0.17(4)
O3	0.3550(2)	0.2733(2)	0.0093(8)	1.0	0.17(4)
C1	0.3189(2)	0.2452(2)	0.4273(7)	1.0	0.86(2)
C2	0.3280(2)	0.2059(2)	0.2857(7)	1.0	0.86(2)
C3	0.3446(2)	0.2211(2)	0.0933(7)	1.0	0.86(2)
C4	0.3521(2)	0.1833(2)	-0.0262(7)	1.0	0.86(2)
H	0.3602(3)	0.1927(3)	-0.170(1)	1.0	1.0(2)
O11	0.468(1)	0.3533(9)	0.272(3)	0.232(5)	1.5(7)
N12	0.5145(4)	0.3915(4)	0.211(2)	0.532(7)	7.9(4)
N13	0.5575(8)	0.4275(8)	0.152(4)	0.232(5)	6.8(7)
N11a	0.4712(6)	0.3560(6)	0.264(2)	0.310(6)	5.5(5)
O13a	0.5599(8)	0.4296(8)	0.151(3)	0.310(6)	3.3(6)

Supplementary Table S4 | Rietveld Refinement (10 K) of $Fe_2(dobdc)(N_2O)_{2.5}$. Fractional atomic coordinates, occupancies, and isotropic displacement parameters obtained from Rietveld refinement (10 K) of the $Fe_2(dobdc)$ dosed with 1.25 N_2O per Fe^{2+}, space group R-3, a = 26.1243(5) Å, c = 6.87522(2) Å, and V = 4063.6(2) Å^3.

Atom	x	y	z	occ.	Uiso*100
Fe	0.3828(2)	0.3518(2)	0.1479(6)	1.0	0.95(9)
O1	0.3271(3)	0.2952(3)	0.3619(9)	1.0	0.32(7)
O2	0.3006(3)	0.2252(3)	0.593(1)	1.0	0.32(7)
O3	0.3554(3)	0.2736(3)	0.006(1)	1.0	0.32(7)
C1	0.3194(2)	0.2471(3)	0.4234(9)	1.0	0.81(4)
C2	0.3267(3)	0.2057(3)	0.2872(8)	1.0	0.81(4)
C3	0.3457(2)	0.2223(3)	0.0956(9)	1.0	0.81(4)
C4	0.3507(3)	0.1808(3)	-0.0232(9)	1.0	0.81(4)
H	0.3632(5)	0.1931(4)	-0.169(2)	1.0	1.35(3)
O11	0.4704(7)	0.3515(9)	0.249(4)	0.320(8)	3.7(9)
N12	0.5176(3)	0.3919(3)	0.213(1)	0.639(9)	5.4(4)
N13	0.5610(5)	0.4309(7)	0.164(3)	0.320(8)	4.9(6)
N11a	0.4711(5)	0.3630(7)	0.268(2)	0.308(8)	1.4(4)
N13a	0.5657(6)	0.4187(16)	0.142(4)	0.308(8)	10.4(8)
N21	0.1468(8)	0.1587(8)	0.605(3)	0.383(5)	10.0(8)
N22	0.1620(7)	0.1862(7)	0.462(3)	0.383(5)	8.0(7)
O23	0.1744(1)	0.2166(9)	0.331(3)	0.383(5)	3.8(7)
N11aa	0.5090(6)	0.3732(7)	0.333(2)	0.310(5)	2.4(5)
O11aa	0.559(1)	0.403(1)	0.402(4)	0.310(5)	0.7(6)
N11ab	0.4619(8)	0.3481(8)	0.285(3)	0.310(5)	3.7(6)

Supplementary Table S5 | Rietveld Refinement (100 K) of $Fe_2(OH)_2(dobdc)$. Space group R-3, a = 25.6125(2) Å, c = 6.8036(1) Å, and V = 3865.20(8) $Å^3$. This data was obtained from 11-BM at the Advanced photon source at Argonne National Laboratory using a wavelength of 0.7291 Å**.**

Atom	x	y	z	occ.	Uiso*100
Fe	0.3893(1)	0.3510(1)	0.1539(3)	1.0	2.95*
O1	0.3230(3)	0.2972(4)	0.356(1)	1.0	2.3(2)
O2	0.3009(4)	0.2289(3)	0.594(1)	1.0	2.3(2)
O3	0.3553(3)	0.2727(4)	0.000(1)	1.0	2.3(2)
C1	0.3164(8)	0.2467(6)	0.415(2)	1.0	1.1(2)
C2	0.3260(6)	0.2052(7)	0.288(2)	1.0	1.1(2)
C3	0.3431(5)	0.2202(7)	0.092(2)	1.0	1.1(2)
C4	0.3492(6)	0.1795(7)	-0.044(2)	1.0	0.9(2)
OH	0.4524(4)	0.3473(5)	0.294(1)	1.0	8.66*

*Uaniso Fe = $[U_{11},U_{22},U_{33},U_{12},U_{13},U_{23}]$ = [4.0(2),1.9(2),1.7(1),0.5(2),0.4(2),0.4(2)];
Uaniso Ox = $[U_{11},U_{22},U_{33},U_{12},U_{13},U_{23}]$ = [7(1),15(1),8(1),10(1),0.00,0.00]

Supplementary Table S6 | Rietveld Refinement (298 K) of the $Fe_2(OH)_2$(dobdc).
Space group R-3, a = 25.6191(2) Å, c = 6.8042(1) Å, and V = 3867.55(9) $Å^3$

Atom	x	y	z	occ.	Uiso*100 ($Å^2$)
Fe	0.3897(1)	0.3512(1)	0.1540(4)	1.0	3.14*
O1	0.3222(4)	0.2967(4)	0.358(1)	1.0	2.6(2)
O2	0.3005(4)	0.2295(4)	0.596(1)	1.0	2.6(2)
O3	0.3553(4)	0.2736(4)	-0.004(2)	1.0	2.6(2)
C1	0.3167(8)	0.2473(7)	0.416(2)	1.0	1.6(2)
C2	0.3265(6)	0.2051(7)	0.294(2)	1.0	1.6(2)
C3	0.3431(6)	0.2219(7)	0.101(2)	1.0	1.6(2)
C4	0.3488(6)	0.1815(7)	-0.039(2)	1.0	1.6(2)
Ox	0.4528(5)	0.3489(6)	0.297(1)	1.0	12.2*

*Uaniso Fe = [U_{11},U_{22},U_{33},U_{12},U_{13},U_{23}] = [4.4(2),1.8(2),1.5(1),0.3(2),0.5(2),-0.3(2)];
Uaniso Ox = [U_{11},U_{22},U_{33},U_{12},U_{13},U_{23}] = [8(1),27(2),9(1),14(1),0.00,0.00]

Supplementary Table S7 | EXAFS curve fitting parameters for Fe_2(dobdc) and comparison with bond lengths obtained by PXRD.

Path	R (Å)		N	σ^2 (Å^2)	R (%)
	PXRD	EXAFS			
Fe–O	2.10*a*	2.06(1)	**5**	0.010(2)	1.0
Fe–C	3.05*a*	3.07(5)	**5**	0.003(4)	$\Delta E_0 = 3.1$
Fe–Fe	3.00(2)	2.96(3)	**2**	0.010(6)	
Fe–OC	3.23*a*	3.22(8)	**10**	0.010(11)	

Supplementary Table S8 | EXAFS curve fitting parameters for 2 and comparison with bond lengths obtained by DFT (periodic PBE+U) and PXRD (100 K data). Note that although the PXRD and EXAFS are in good agreement overall, there are dissimilarities, especially in the Fe–O_{axial} bond lengths for **2**. This is because while EXAFS can be used to obtain first-shell distances with great accuracy, it is much more limited when resolution of different bond lengths is needed, especially when the scatterers have both a similar distance and atomic number, as is the case in **2**.[30]

Path	R (Å)			N	σ^2 (Å^2)	R (%)
	DFT	PXRD	EXAFS			
Fe–OH	1.84	1.92(1)	1.85(3)	**1**	0.009(1)	1.1
Fe–O_{eq}	2.02*a*	2.04*a*	2.02(1)	**4**	0.009(1)	$\Delta E_0 = 2.70$
Fe–O_{ax}	2.27	2.20(1)	2.33(4)	**1**	0.009(1)	
Fe–C	3.01*a*	3.03*a*	2.95(7)	**5**	0.009(1)	
Fe–Fe	3.23	3.16(1)	3.15(9)	**2**	0.016(4)	
Fe–O–C	3.19*a*	3.21*a*	3.16(14)	**10**	0.006(8)	

Bold numbers are fixed values.

Numbers in parentheses show uncertainty.

a Averaged values.

Supplementary Table S9 | Mössbauer spectral parameters.

Sample	δ, mm/s	$\|\Delta E_Q\|$, mm/s	Γ, mm/s	Area (%)	Assignment
$Fe_2(OH)_2(dobdc)$ (**1**)	0.40(2)	0.96(1)	0.34(1)	80(2)	Fe^{III}–OH
	0.40(2)	1.80(6)	0.50(1)	13(2)	Unknown Fe^{III}
	1.21(6)	1.77(9)	0.57(15)	7(2)	Fe^{II}
$Fe_2(OH)_{0.6}(dobdc)$ (**1'**)	0.44(2)	0.95(4)	0.41(4)	30(3)	Fe^{III}–OH
	1.08(1)	1.98(2)	0.44(3)	70(4)	Fe^{II}
$Fe_{0.1}Mg_{1.9}(dobdc)$ (**2**)	1.08(1)	2.25(1)	0.31(2)	100	Fe^{II}
$Fe_{0.1}Mg_{1.9}(dobdc)$	0.45(1)	1.08(3)	0.51(2)	89(4)	Fe^{III}–OH
(after N_2O/C_2H_6 treatment)	1.07(7)	2.24(11)	0.34(12)	11(3)	Fe^{II}

Supplementary Table S10 | Unit cell parameters (298 K) of $Fe_2(dobdc)$, $Fe_xMg_{2-x}(dobdc)$, and $Mg_2(dobdc)$. The unit cell constants and volumes of $Fe_{0.1}Mg_{1.9}(dobdc)$ and $Fe_{0.44}Mg_{1.56}(dobdc)$ are in between that of $Fe_2(dobdc)$ and $Mg_2(dobdc)$[31] and show a linear correlation with magnesium content, in agreement with Vegard's Law for solid solutions.

	$Fe_2(dobdc)$	**$Fe_{0.44}Mg_{1.56}(dobdc)$**	**$Fe_{0.1}Mg_{1.9}(dobdc)$**	**$Mg_2(dobdc)$**
***a* (Å)**	26.1603(10)	25.9964(8)	25.9485(9)	25.9111(20)
***c* (Å)**	6.8657(4)	6.8465(4)	6.8574(4)	6.8687(12)
***V* (Å^3)**	4069.1(3)	4007.1(4)	3998.7(3)	3993.7(7)

Supplementary Table S11 | Relative energies (kJ/mol)[a] and Mulliken atomic spin densities on Fe and O1[b] for 2 and 4. Full geometry optimizations were performed by periodic PBE+U for three possible spin states of each **2** and **4**.

Species	2*S*	Spin density on Fe	Spin density on O1	Fe–O1 Distance(Å)	Relative energy (kJ/(mol Fe))[a]
2	1	1.09	0.00	1.81	149.5
	3	3.34	–0.15	1.87	61.7
	5	4.31	0.23	1.84	0.0
4	0	0.00	0.00	1.64	113.9
	2	1.51	0.46	1.62	76.7
	4	3.42	0.33	1.64	0.0

[a] The lowest-energy spin state for each species has been taken as 0 reference.

[b] O1 is the terminal oxygen as shown in Figure S19.

Supplementary Table S12 | Relative energies (kJ/mol)[a], S, S^2, and Mulliken spin densities on Fe and O1 for 2 and 4 cluster models. Single-point calculations were done on the 89- and 90-atom models using PBE/SDD(Fe, Zn), 6-311+G(2df,p)(C, H, O)//PBE/SDD(Fe, Zn),6-31G(d)(C, H, O).

Species	State			Spin density		Relative energy
	$2M_S$	S	S^2	Fe	O1	(kJ/mol)[a]
2 (cluster model)	1	0.67	1.12	0.97	0.13	52.1
	3	1.52	3.82	2.88	0.03	32.6
	5	2.50	8.76	4.27	0.34	0.0
4 (cluster model)	0 (open shell)	0.79	1.42	–0.08	0.07	88.4
	2	1.06	2.20	1.57	0.73	54.4
	4	2.01	6.06	3.08	0.60	0.0
	6	3.01	12.01	3.97	1.16	104.8

[a]Relative energy is computed with respect to the most stable spin state.

Supplementary Table S13 | Relative energies (kJ/mol)[a], S, S^2, and Mulliken spin densities on Fe and O1 for 2 and 4 cluster models. Single-point calculations were done on the 89- and 90-atom models using M06/SDD(Fe, Zn), 6-311+G(2df, p)(C, H, O)//M06-L/SDD(Fe, Zn),6-31G(d)(C, H, O).

Species	State			Spin density		Relative energy
	$2M_S$	S	S^2	Fe	O1	(kJ/mol)[a]
2 (cluster model)	1	0.85	1.56	1.05	0.04	218.5
	3	1.53	3.87	3.11	–0.13	109.6
	5	2.50	8.76	4.30	0.30	0.0
4 (cluster model)	0 (open shell)	0.99	1.96	1.00	–1.10	210.6
	2	1.24	2.76	2.83	–0.39	136.4
	4	2.05	6.28	3.65	0.31	0.0
	6	3.00	12.03	4.16	1.15	57.2

[a]Relative energy is computed with respect to the most stable spin state.

Supplementary Table S14 | Relative energies (kJ/mol)[a], S, S^2, and Mulliken spin densities on Fe and O1 for 2 and 4 cluster models. Single-point calculations were done on the 89- and 90-atom models using M08-SO/SDD(Fe, Zn),6-311+G(2df,p)(C, H, O)//M06-L/SDD(Fe, Zn),6-31G(d)(C, H, O).

Species	State			Spin density		Relative energy
	$2M_S$	S	S^2	Fe	O1	(kJ/mol)[a]
2 (cluster model)	1	1.01	2.02	1.02	0.01	115.8
	3	1.51	3.79	2.98	–0.07	82.5
	5	2.50	8.76	4.37	0.33	0.0
4 (cluster model)	0 (open shell)	1.03	2.09	–0.99	1.02	124.2
	2	1.31	3.03	2.78	–0.87	86.8
	4	2.06	6.29	3.73	0.13	0.0
	6	3.00	12.02	4.28	1.34	55.3

[a]Relative energy is computed with respect to the most stable spin state.

Supplementary Table S15 | Relative energies (kJ/mol)[a], S, S^2, and Mulliken spin densities on Fe and O1 for 2 and 4 cluster models. Single-point calculations were done on the 89- and 90-atom models using MPW1B95/SDD(Fe, Zn), 6-311+G(2df, p)(C, H, O)//M06-L/SDD(Fe, Zn), 6-31G(d)(C, H, O).

Species	State			Spin density		Relative energy
	$2M_S$	S	S^2	Fe	O1	(kJ/mol)[a]
2 (cluster model)	1	0.60	0.96	1.04	0.06	143.5
	3	1.53	3.88	3.07	–0.13	80.1
	5	2.50	8.76	4.34	0.29	0.0
4 (cluster model)	0 (open shell)	0.80	1.44	0.72	–0.61	141.7
	2	1.24	2.79	2.87	–0.58	96.1
	4	2.06	6.29	3.69	0.14	0.0
	6	3.00	12.02	4.21	1.20	45.3

[a]Relative energy is computed with respect to the most stable spin state.

Supplementary Table S16 | Relative energies (kJ/mol)[a], S, S^2, and Mulliken spin densities on Fe and O1 for 2 and 4 cluster models. Single-point calculations were done on the 89- and 90-atom models using PW6B95/SDD(Fe, Zn), 6-311+G(2df, p)(C, H, O)//M06-L/SDD(Fe, Zn), 6-31G(d)(C, H, O).

Species	State			Spin density		Relative energy
	$2M_S$	S	S^2	Fe	O1	(kJ/mol)[a]
2 (cluster model)	1	0.60	0.96	1.03	0.07	121.4
	3	1.53	3.87	3.04	–0.11	69.7
	5	2.50	8.76	4.32	0.30	0.0
4 (cluster model)	0 (open shell)	0.80	1.43	0.64	–0.54	126.8
	2	1.23	2.74	2.79	–0.43	87.4
	4	2.05	6.25	3.61	0.25	0.0
	6	3.00	12.03	4.18	1.17	50.3

[a] Relative energy is computed with respect to the most stable spin state.

Supplementary Table S17 | Calculated relative energies (kJ/mol) for N_2O bound to the Fe(II) site of the 88-atom cluster. The relative energies of η^1-N and η^1-O coordination modes are computed using M06-L and M06 density functionals with the def2-TZVP and SDD(Fe, Zn), 6-31G(d)(C, H, O, N) basis sets. The level of optimization is opt6.

Functional	Binding mode	SDD(Fe, Zn), 6-31G(d)(C, H, O, N)	def2-TZVP
M06-L	η^1-O	0.0	0.0
	η^1-N	–4.6	–9.5
M06	η^1-O	0.0	0.0
	η^1-N	1.1	–4.5

Supplementary Table S18 | State energy splitting of 2 and 4 cluster models calculated by CASSCF and CASPT2.

Species	$2M_S$	Largest CASSCF configuration weight	M^a	Relative CASSCF energy (kJ/mol)	Relative CASPT2 energy (kJ/mol)
2 (cluster model)	1	94%	0.102	328.4	294.6
	3	79%	0.309	216.7	145.2
	5	100%	0.000	0.0	0.0
4 (cluster model)	0(open shell)	77%	0.272	210.5	249.4
	2	74%	0.306	139.3	127.6
	4	77%	0.311	0.0	0.0

[a] M is a diagnostic used to quantify the extent of multireference character of the system, and it is defined to be

$$M = \frac{1}{2}\left(2 - n(\mathrm{MCDONO}) + \sum_{j=1}^{n_{\mathrm{SOMO}}} \left| n(j) - 1 \right| + n(\mathrm{MCUNO}) \right)$$

where $n(\mathrm{MCDONO})$, n_{SOMO}, and $n(\mathrm{MCUNO})$ are the most correlated doubly occupied natural orbital, a singly occupied natural orbital, and the most correlating unoccupied natural orbital, respectively. Additional details of this metric may be found in a work by Tishchenko *et al*.[32]

Supplementary Table S19 | Charge and spin densities of the sextet and quintet ground spin states of the cluster models of 2 and 4 from CASSCF calculations.

	2 (cluster model)		4 (cluster model)	
	Fe	**O1**	**Fe**	**O1**
CASSCF Mulliken Spin Density	4.79	0.07	3.744	0.173
CASSCF Mulliken Charge Density	1.95	–0.77	1.765	–0.419
CASSCF LoProp Charge Density	2.21	–1.09	1.963	–0.559

Supplementary Table S20 | Relative energies (kJ/mol)[a], S, S^2, and Mulliken spin densities on Fe and O1 for the cluster model of 4 and the cluster model of 4 with Zn(II) replacing Mg(II). All calculations were done using M06-L/SDD(Fe, Zn), 6-31G(d)(C, H, O, Mg)/opt6.

Species	**State**			**Spin density**		**Fe–O1**	**Relative energy**
	$2M_S$	S	S^2	Fe	O1	**(Å)**	**(kJ/mol)[a]**
4	0	0.77	1.36	0.27	–0.14	1.62	138.2
(cluster model	2	1.15	2.48	2.02	0.44	1.61	77.3
with Zn(II))	4	2.04	6.22	3.31	0.60	1.64	0.0
4	0	0.78	1.40	0.26	–0.11	1.62	138.7
(cluster model	2	1.17	2.55	2.18	0.34	1.60	71.9
with Mg(II))	4	2.06	6.29	3.35	0.61	1.64	0.0

[a]Relative energy is computed with respect to the most stable spin state.

Supplementary Table S21 | Relative energies (kJ/mol)[a], S, S^2, and Mulliken spin densities on Fe and O1 for the cluster model of 4 and the cluster model of 4 with Zn(II) replacing Mg(II). All calculations were done using M06/SDD(Fe, Zn), 6-31G(d)(C, H, O, Mg)/opt6.

Species	**State**			**Spin density**		**Fe–O1**	**Relative energy**
	$2M_S$	S	S^2	Fe	O1	**(Å)**	**(kJ/mol)[a]**
4	0	0.86	1.60	0.41	–0.47	1.58	213.3
(cluster model	2	1.27	2.90	2.90	–0.32	1.62	132.1
with Zn(II))	4	2.05	6.27	3.54	0.42	1.63	0.0
4	0	0.91	1.73	–0.60	0.58	1.59	215.6
(cluster model	2	1.29	2.97	2.91	–0.24	1.62	125.0
with Mg(II))	4	2.07	6.38	3.61	0.46	1.64	0.0

[a]Relative energy is computed with respect to the most stable spin state.

Supplementary Table S22 | Binding energies[a] (kJ/mol) of η^1-N and η^1-O coordination modes of N_2O bound to the iron(II) site of the 88-atom cluster. The calculations were done using M06-L and M06 density functionals with SDD(Fe, Zn), 6-31G(d)(C, H, O, N) basis set. The level of optimization is opt6.

Functional	Binding mode	Binding energy (kJ/mol)
M06-L	η^1-O	41.4
	η^1-N	46.1
M06	η^1-O	45.6
	η^1-N	44.5

[a]Binding Energy = E(cluster) + E(N_2O) – E(complex)

Supplementary Table S23 | Natural bond analysis of η^1-N and η^1-O coordination modes of N_2O bound to the iron(II) site of the 88-atom cluster.

Binding mode	% Back-bonding
η^1-O	42%
η^1-N	43%

4. Supplemental Figures

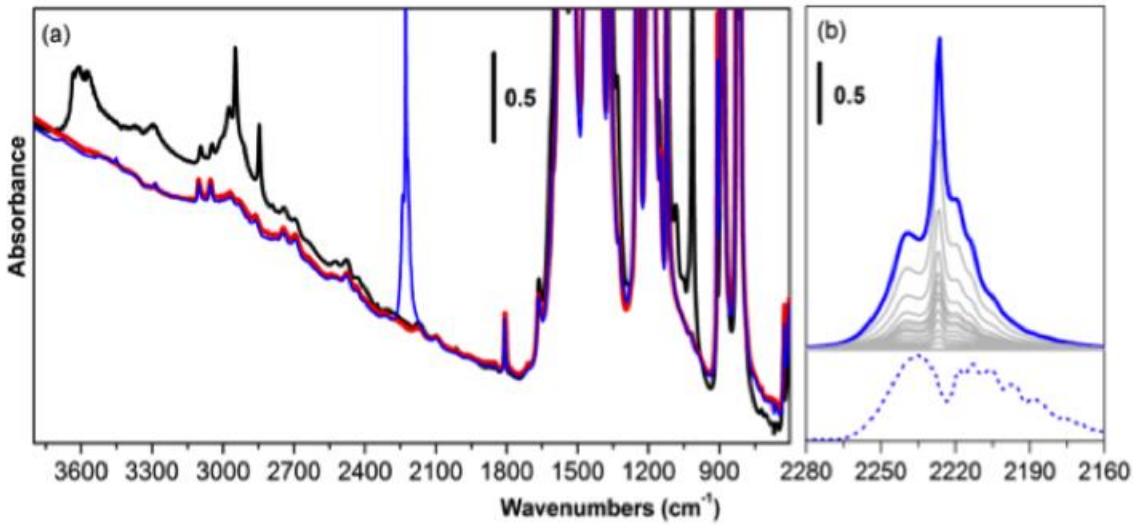

Supplementary Figure S1 | *In situ* transmission-mode FTIR spectra of Fe_2(dobdc) demonstrating reversible N_2O binding at room temperature. a. FTIR spectra of Fe_2(dobdc) outgassed at room temperature 2 h (black curve) and activated at 433 K for 18 h (red curve) and in contact with 40 mbar of N_2O at room temperature (blue curve). The spectrum of the activated sample clearly shows the disappearance of all features associated with methanol, with all other bands unchanged. **b.** FTIR spectra (background subtracted) in the 2280–2160 cm^{-1} spectral range of Fe_2(dobdc) in contact with 40 mbar of N_2O (blue curve) and following progressive desorption at room temperature (light grey curves). A clear maximum is seen at 2226 cm^{-1}. The dotted blue line represents the spectrum of 40 mbar of gaseous N_2O in the same spectral range.

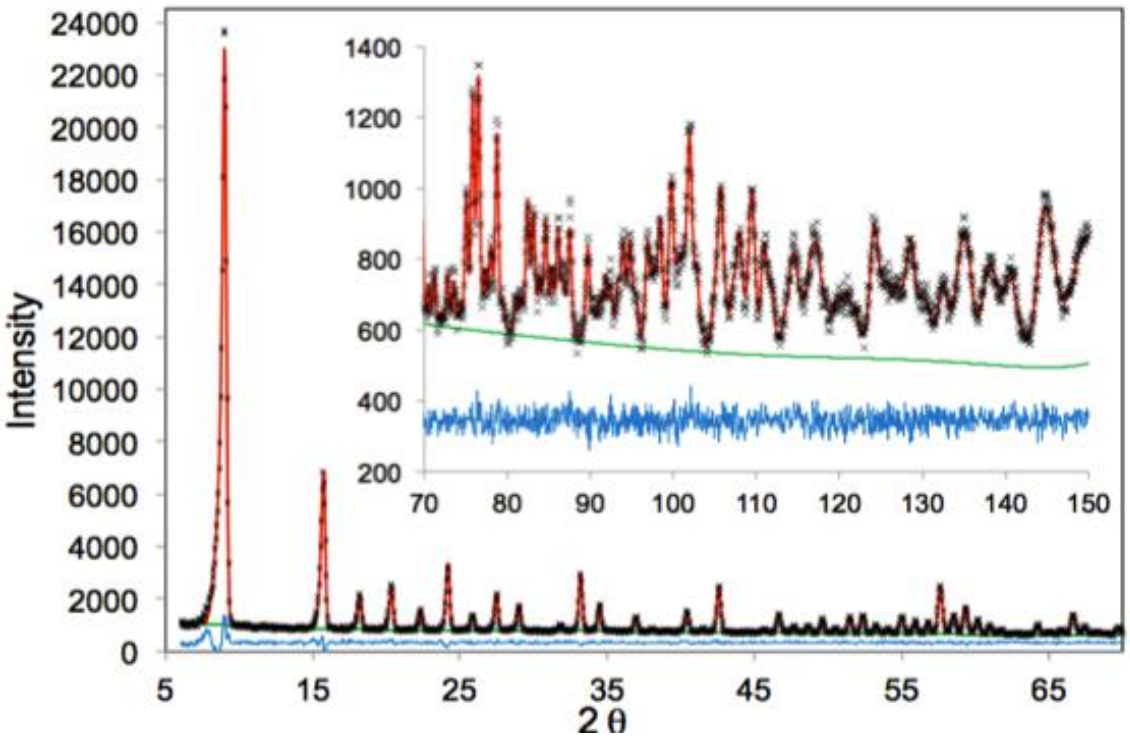

Supplementary Figure S2 | Rietveld refinement (10 K) of bare Fe_2(dobdc). Neutron powder diffraction data obtained from bare Fe_2(dobdc) at 10 K. The green line, crosses, and red line represent the background, experimental, and calculated diffraction patterns, respectively. The blue line represents the difference between experimental and calculated patterns.

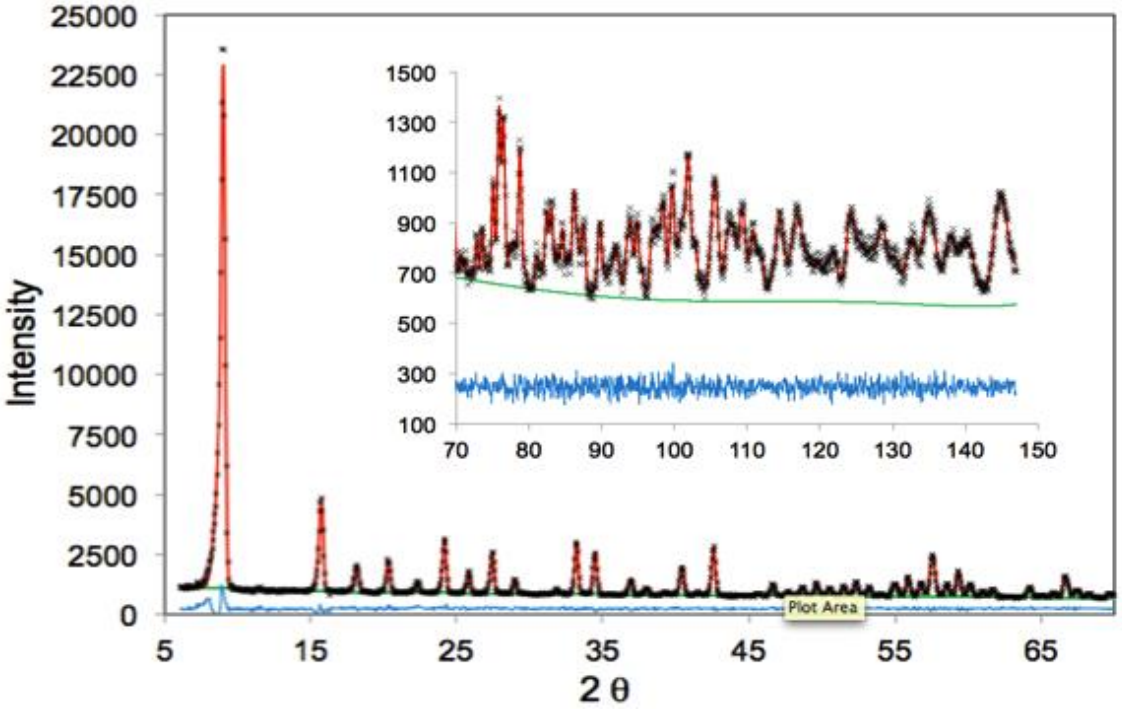

Supplementary Figure S3 | Rietveld refinement (10 K) of $Fe_2(dobdc)(N_2O)_{0.7}$. Neutron powder diffraction data obtained from $Fe_2(dobdc)$ loaded with approximately 0.35 N_2O per Fe^{2+}. The green line, crosses, and red line represent the background, experimental, and calculated diffraction patterns, respectively. The blue line represents the difference between experimental and calculated patterns. The data were collected at 10 K.

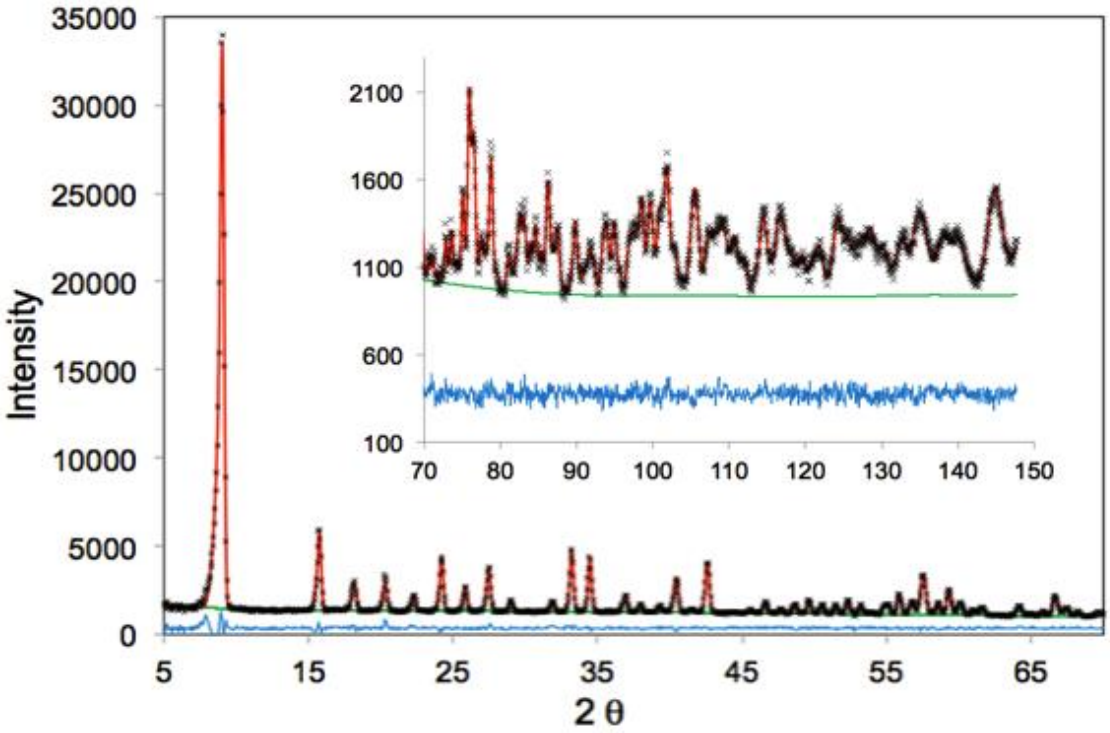

Supplementary Figure S4 | Rietveld refinement (10 K) of $Fe_2(dobdc)(N_2O)_{1.2}$. Neutron powder diffraction data obtained from $Fe_2(dobdc)$ loaded with approximately 0.6 N_2O per Fe^{2+}. The green line, crosses, and red line represent the background, experimental, and calculated diffraction patterns, respectively. The blue line represents the difference between experimental and calculated patterns.

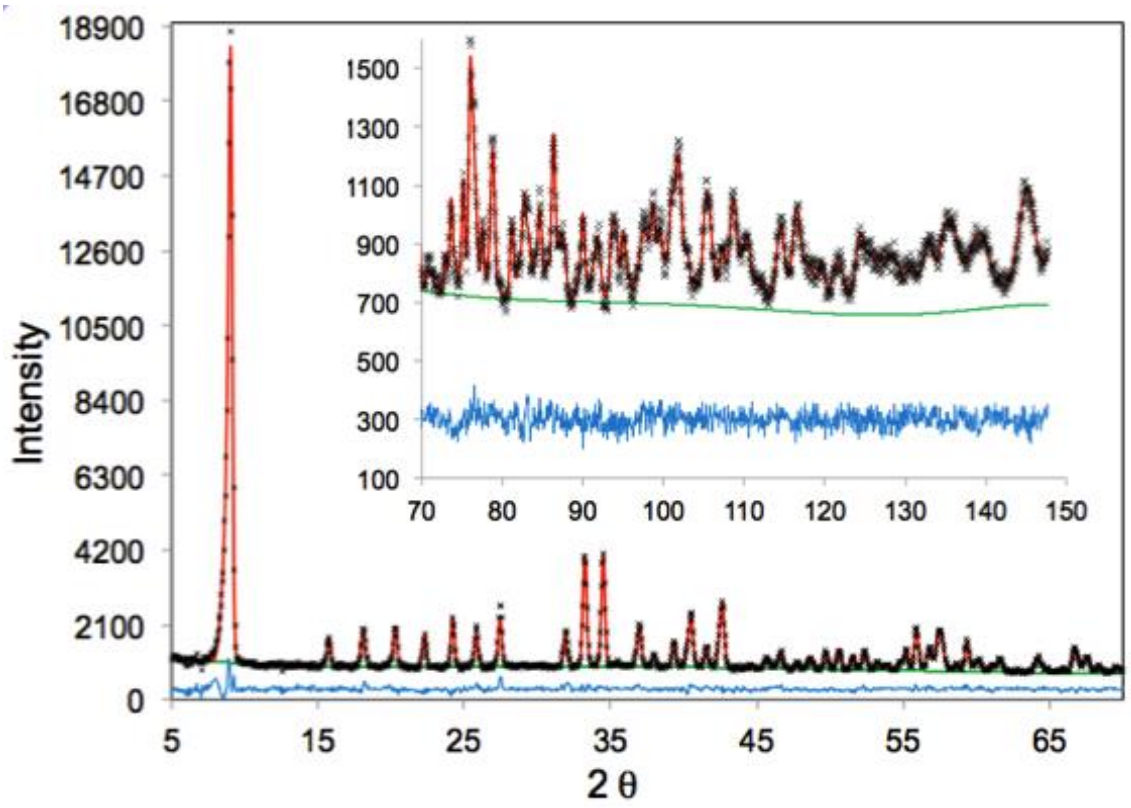

Supplementary Figure S5 | Rietveld refinement (10 K) of $Fe_2(dobdc)(N_2O)_{2.5}$. Neutron powder diffraction data obtained from $Fe_2(dobdc)$ loaded with approximately 1.25 N_2O per Fe^{2+}. The green line, crosses, and red line represent the background, experimental, and calculated diffraction patterns, respectively. The blue line represents the difference between experimental and calculated patterns. The data were collected at 10 K.

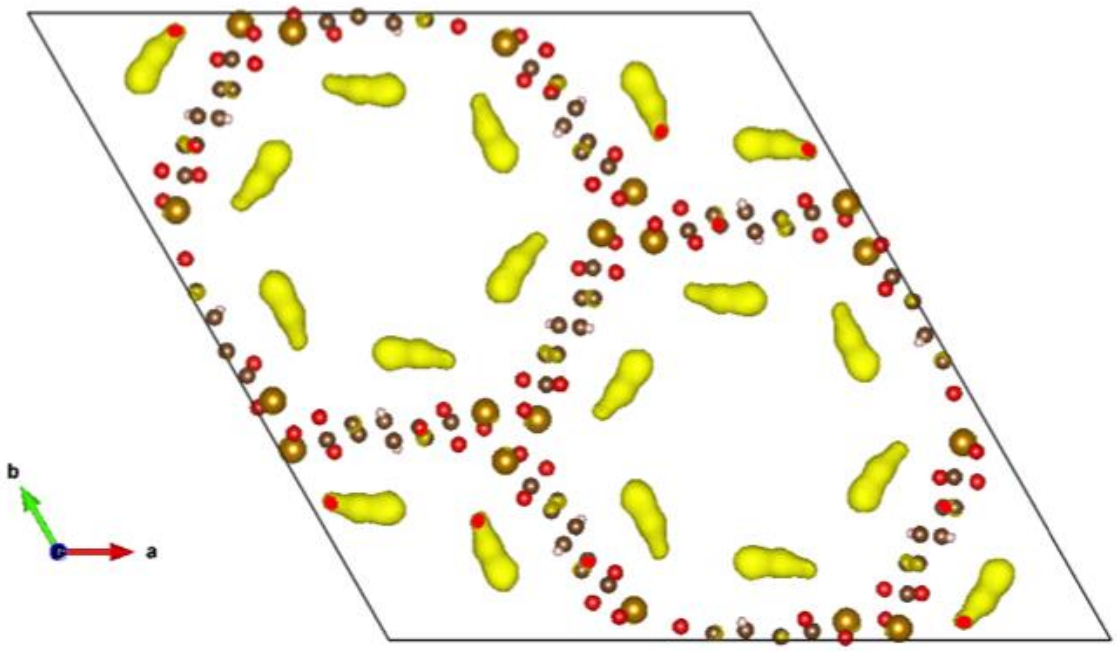

Supplementary Figure S6 | Fourier difference map of $Fe_2(dobdc)(N_2O)_{0.6}$. Fourier Difference Map of data obtained from $Fe_2(dobdc)$ loaded with 0.35 N_2O per Fe^{2+}. Yellow globules represent excess scattering density in the channels of the framework that result from N_2O molecules binding at the Fe^{2+} site.

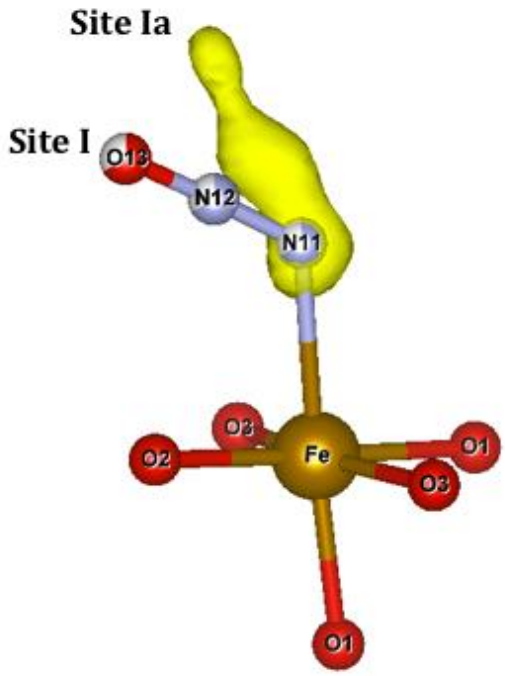

Supplementary Figure S7 | Fourier difference map of $Fe_2(dobdc)(N_2O)_{2.5}$. Fourier Difference Map of data obtained from $Fe_2(dobdc)$ loaded with 1.25 N_2O per Fe^{2+}. Yellow globules represent excess scattering density in the channels of the framework that result from N_2O molecules binding at the Fe^{2+} site. There is a slight rearrangement from the site I N_2O orientation, denoted site Ia, upon population of the secondary adsorption site.

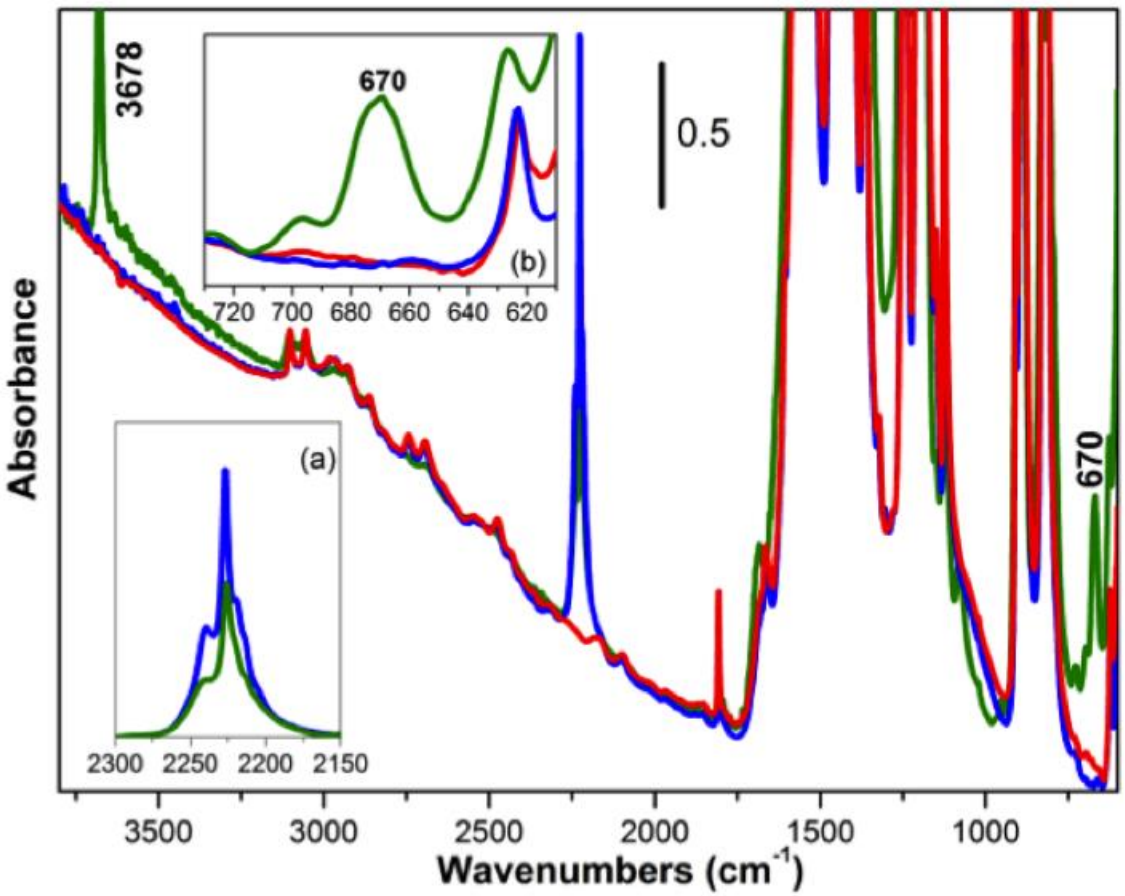

Supplementary Figure S8 | *In situ* transmission-mode FTIR spectra of Fe_2(dobdc) (green) and $Fe_2(OH)_2$(dobdc) (red). A thin film of Fe_2(dobdc) was activated at 433 K for 18 h (red curve), in contact with 180 mbar of N_2O at room temperature (blue curve) and heated at 60 °C for 14 hours (green curve). Inset (a): background subtracted spectra illustrating the ν(N–N) region and inset (b) magnification of 730–610 cm^{-1} spectral range, testifying the formation of $Fe_2(OH)_2$(dobdc).

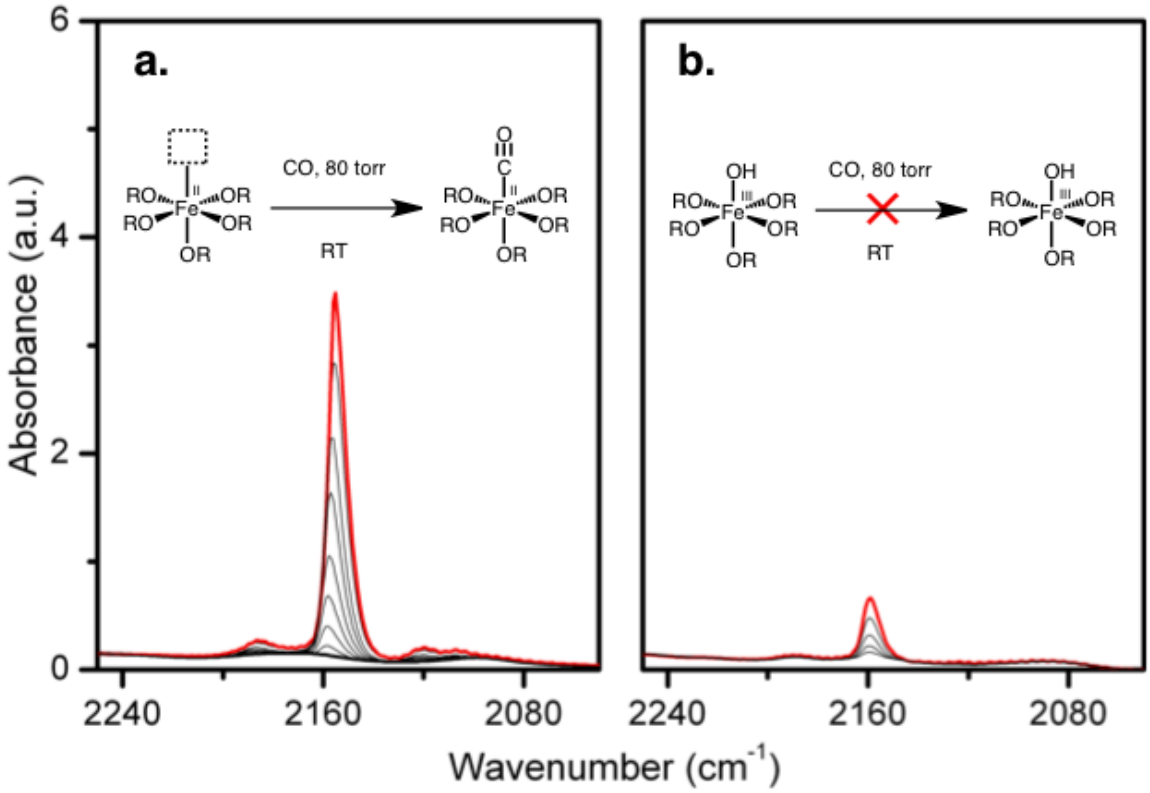

Supplementary Figure S9 | CO titration experiments before and after heating Fe_2(dobdc) in the presence of N_2O. a. CO dosed on an activated sample of bare Fe_2(dobdc). **b.** CO dosed on a sample that has contacted N_2O at room temperature for one day, and then overnight at 60 °C shows that the number of open Fe(II) sites has been reduced dramatically (less than 10% remaining).

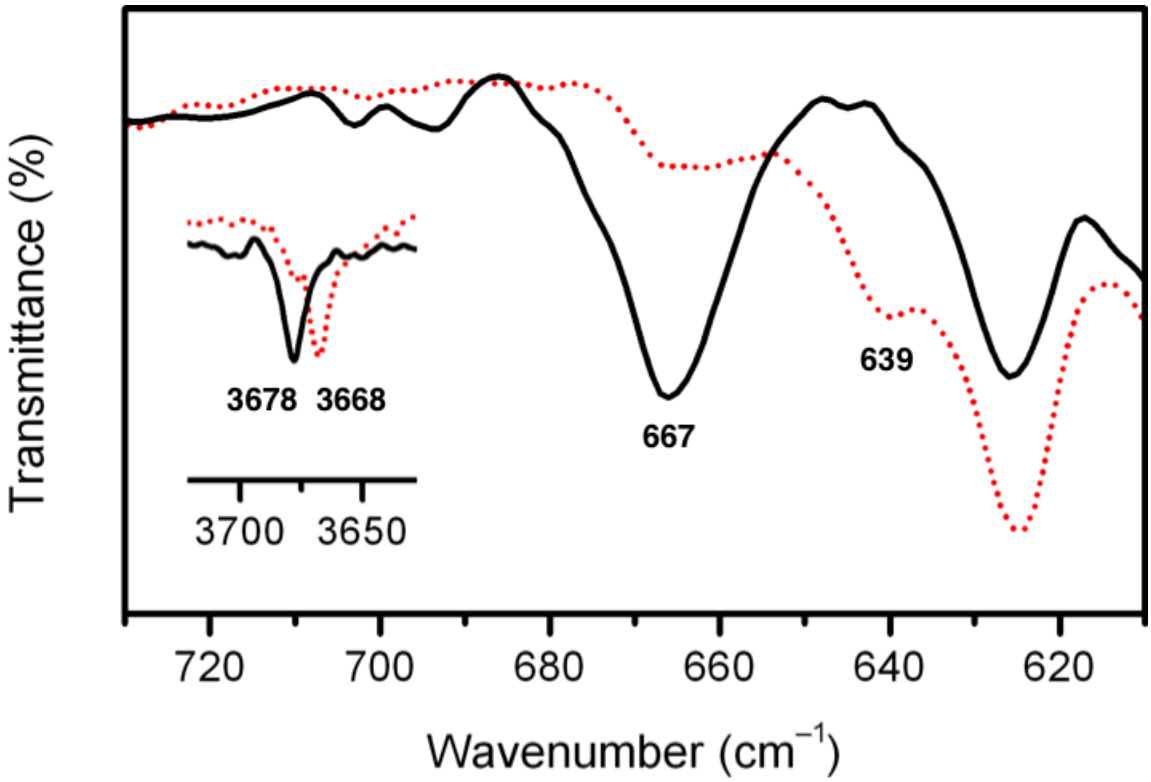

Supplementary Figure S10 | ATR-FTIR spectra of $Fe_2(OH)_{0.6}$(dobdc) (black) and $Fe_2(^{18}OH)_{0.6}$(dobdc) (dotted red).

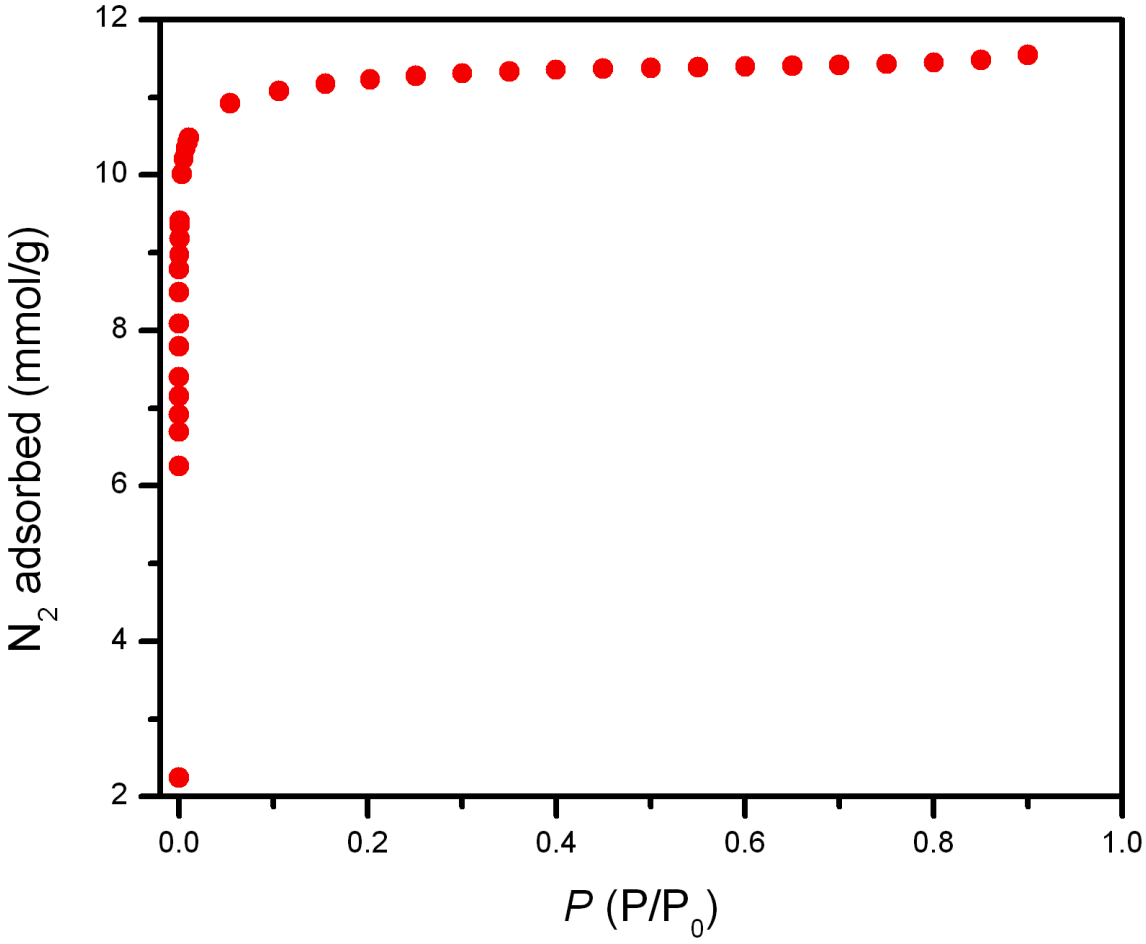

Supplementary Figure S11 | N_2 Adsorption isotherm in $Fe_2(OH)_2(dobdc)$ at 77 K.

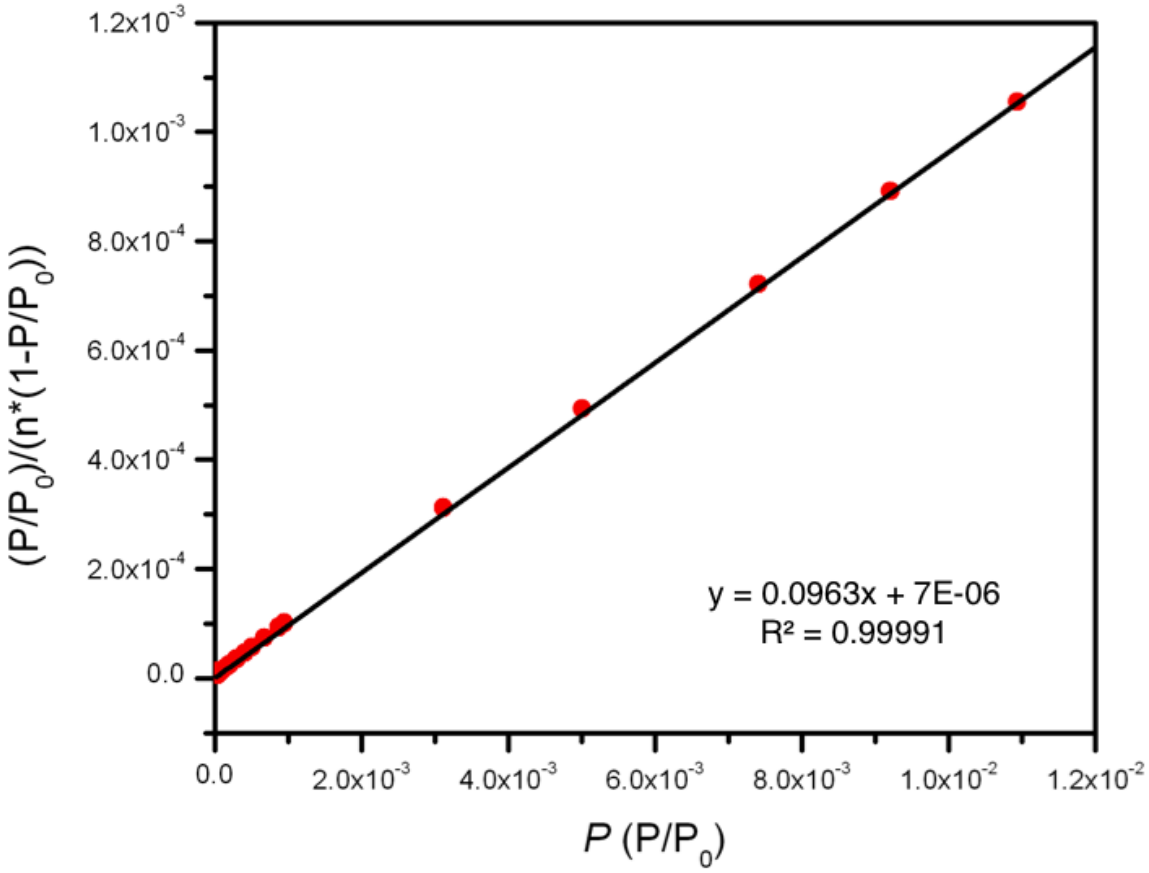

Supplementary Figure S12 | BET plot of the N_2 adsorption isotherm in $Fe_2(OH)_2$(dobdc) at 77 K. The black line represents a linear best fit of the data points (red circles). Inset: parameters for the linear best fit and resulting constants for calculation of the BET surface area.

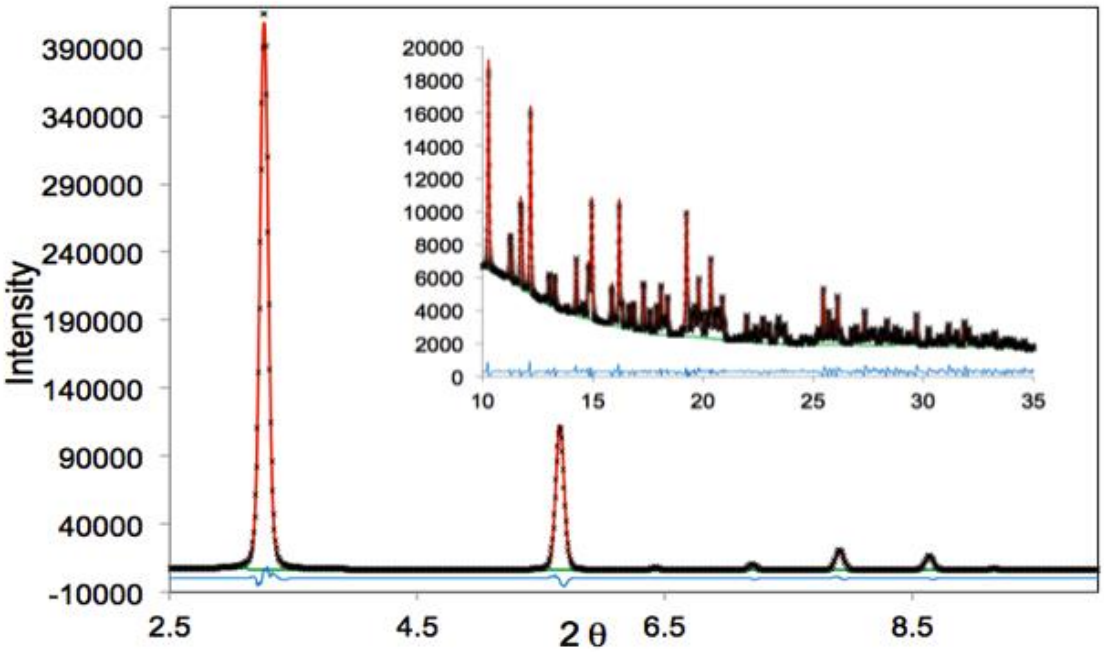

Supplementary Figure S13 | Rietveld refinement (100 K) of $Fe_2(OH)_2$(dobdc). X-ray powder diffraction data obtained from a sample of $Fe_2(OH)_2$(dobdc). The green line, crosses, and red line represent the background, experimental, and calculated diffraction patterns, respectively. The blue line represents the difference between experimental and calculated patterns. The data were collected at 100 K.

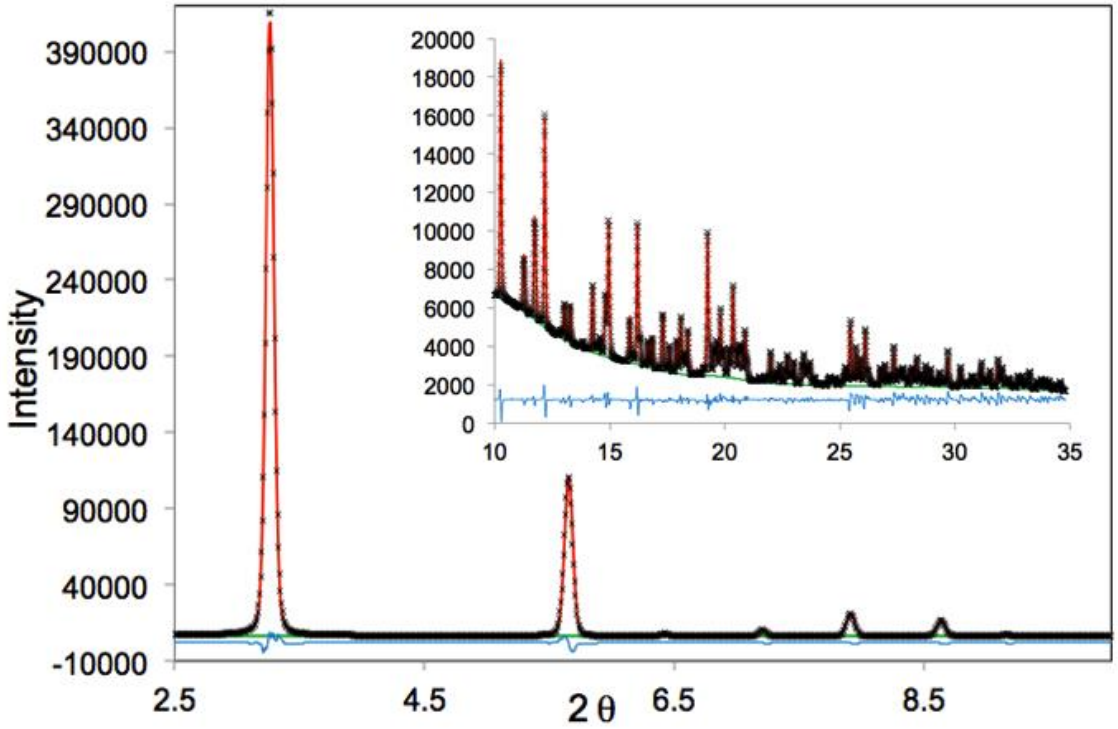

Supplementary Figure S14 | Rietveld refinement (298 K) of $Fe_2(OH)_2$(dobdc). X-ray powder diffraction data obtained from a sample of $Fe_2(OH)_2$(dobdc). The green line, crosses, and red line represent the background, experimental, and calculated diffraction patterns, respectively. The blue line represents the difference between experimental and calculated patterns. The data were collected at 298 K.

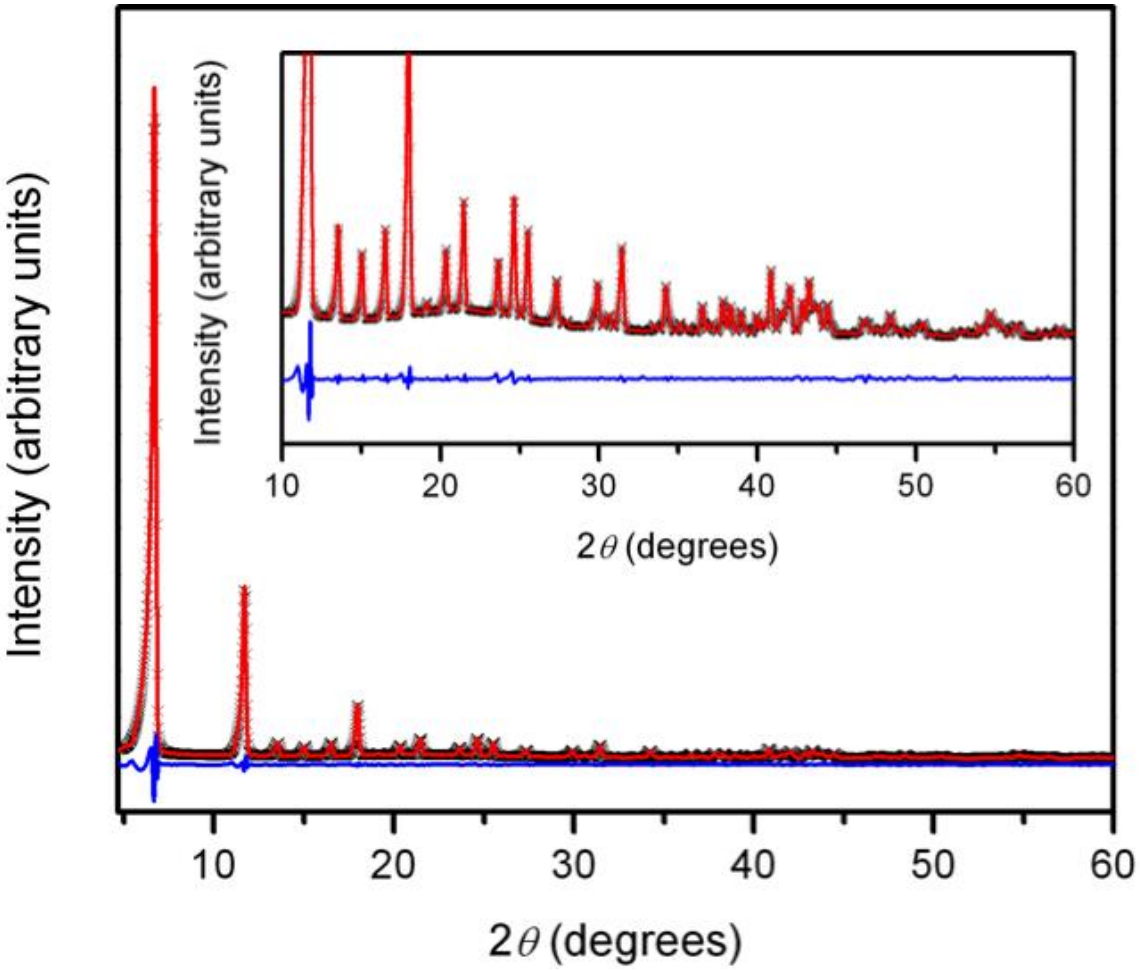

Supplementary Figure S15 | Unit cell of $Fe_{0.1}Mg_{1.9}$(dobdc). X-ray powder diffraction data obtained from a sample of $Fe_{0.1}Mg_{1.9}$(dobdc). a = 25.9485(9) Å, c = 6.8574(4) Å, and V = 3998.7(3) Å^3. The crosses and red line represent the experimental and calculated diffraction patterns, respectively. The blue line represents the difference between experimental and calculated patterns. The data were collected at 298 K.

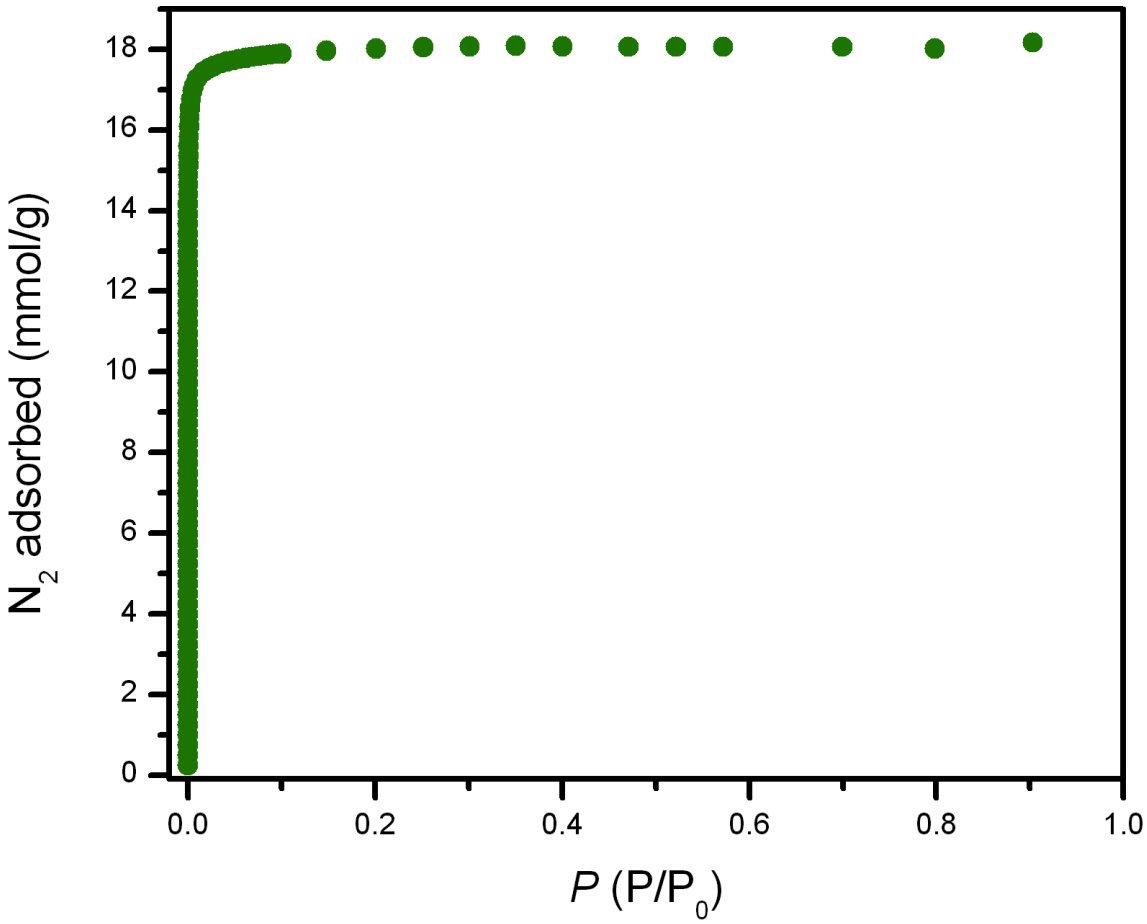

Supplementary Figure S16 | N_2 adsorption isotherm in $Fe_{0.1}Mg_{1.9}$(dobdc) at 77 K.

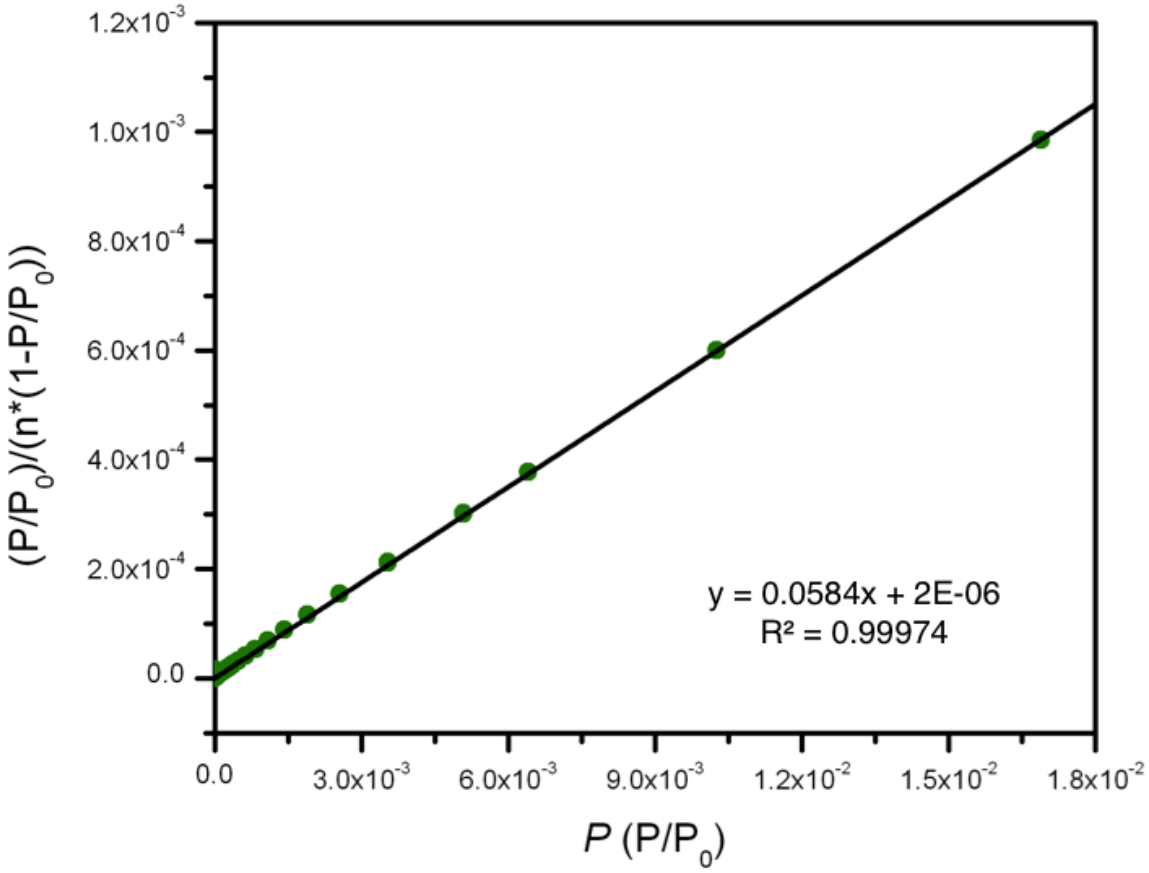

Supplementary Figure S17 | BET plot of the N_2 adsorption isotherm in $Fe_{0.1}Mg_{1.9}$(dobdc) at 77 K. The black line represents a linear best fit of the data points (green circles). Inset: parameters for the linear best fit and resulting constants for calculation of the BET surface area.

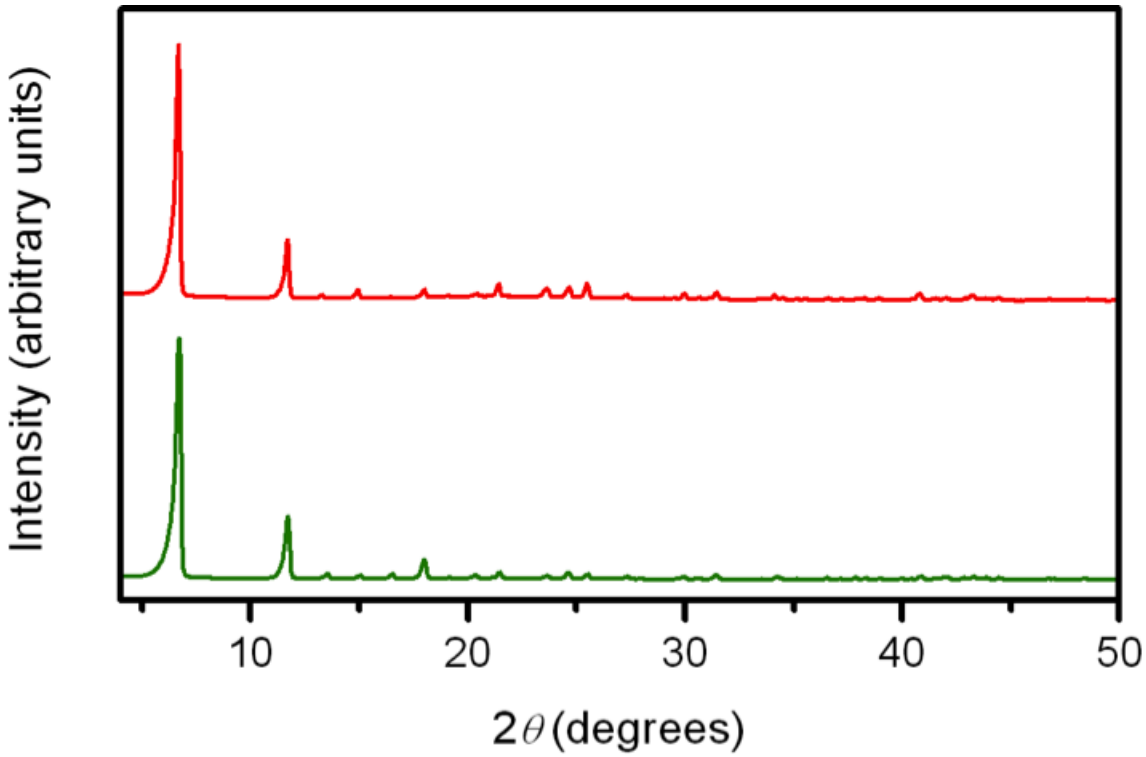

Supplementary Figure S18 | Powder X-ray diffraction patterns for $Fe_{0.1}Mg_{1.9}$(dobdc) before (green) and after (red) N_2O/ethane treatment.

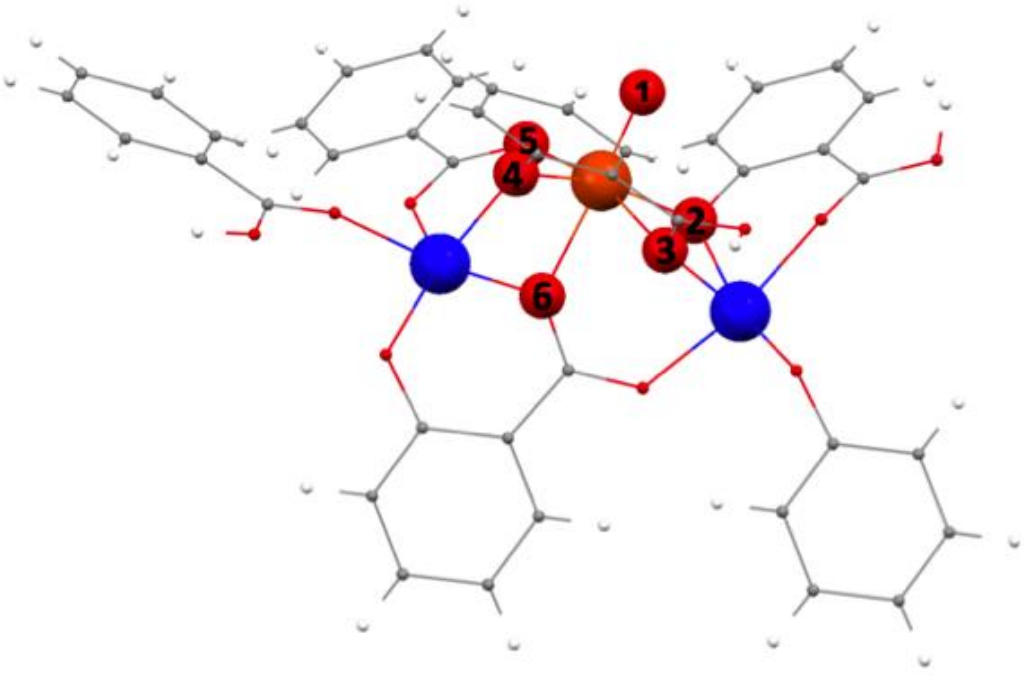

Supplementary Figure S19 | Wireframe representation of the cluster model for 4 (89-atom cluster model). Highlighted in ball and stick, the Fe atom and its first coordination sphere and the Zn centers. The 90-atom cluster model for **2** is similar, except O1 is replaced with an OH. Color code: orange, Fe; blue, Zn; red, O; grey, C and white, H.

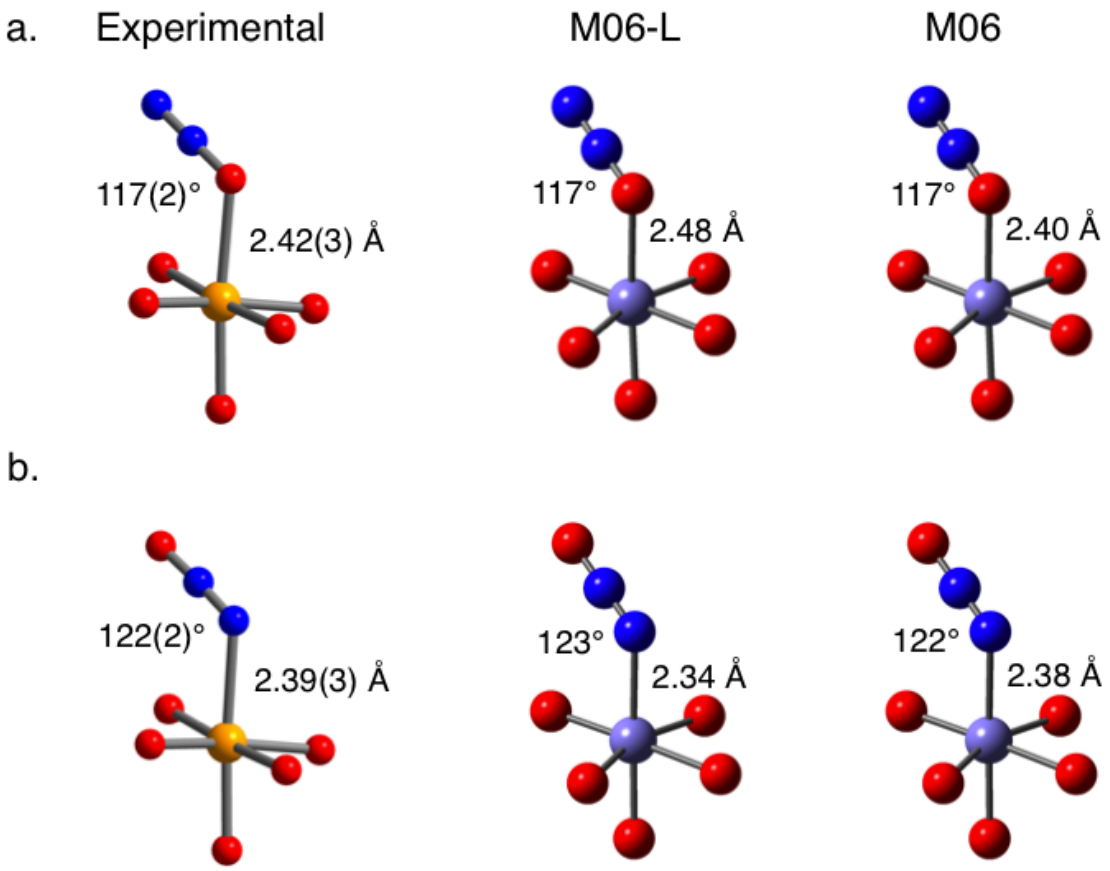

Supplementary Figure S20 | Comparison of the experimental and theoretical structures of the N_2O adducts of Fe_2(dobdc). a. η^1-O coordination of the N_2O molecule. **b.** η^1-N coordination of the N_2O molecule. All distances are in Å and all angles are in degrees. Color code: blue, N; red, O; yellow, Fe (experiment) or purple, Fe (theory).

5. References for Supporting Information

1. (a) Rivallan, M., Ricchiardi, G., Bordiga, S. & Zecchina, A. Adsorption and reactivity of nitrogen oxides (NO_2, NO, N_2O) on Fe–zeolites. *J. Catal*. **264,** 104-116 (2009). (b) Wood, B.R., Reimer, J. A. & Bell, A. T. Studies of N_2O adsorption and decomposition on Fe–ZSM-5. *J. Catal.* **209**, 151–158 (2000).
2. Ion Prisecaru, WMOSS4 Mössbauer Spectral Analysis Software, www.wmoss.org, 2009-2013.
3. (a) A. C. Larson & R. B. Von Dreele. General Structure Analysis System (GSAS). *Los Alamos National Laboratory Report LAUR*, 86-748 (1994). (b) B. H. Toby. EXPGUI, a graphical user interface for GSAS. *J. Appl. Cryst*. **34**, 210-213 (2001).
4. (a) E. D. Bloch, L. J. Murray, W. L. Queen, S. Chavan, S. N. Maximoff, J. P. Bigi, R. Krishna, V. K. Peterson, F. Grandjean, G. J. Long, B. Smit, S. Bordiga, C. M. Brown & J. R. Long. Selective binding of O_2 over N_2 in a redox-active metal-organic framework with open iron(II) coordination sites. *J. Am. Chem. Soc*. **133**, 14814-14822 (2011). (b) W. L. Queen, E. D. Bloch, C. M. Brown, M. R. Hudson, J. A. Mason, L. J. Murray, A. J. Ramirez-Cuesta, V. K. Peterson, and J. R. Long. Hydrogen adsorption in the metal-organic frameworks Fe_2(dobdc) and $Fe_2(O_2)$(dobdc). *Dalt. Trans*. **41**, 4180-4187 (2012).
5. V. F. Sears. Neutron scattering lengths and cross sections. *Neutron News*, **3**, 26-37 (1992).
6. Coelho, A. Indexing of powder diffraction patterns by iterative use of singular value decomposition. *J. Appl. Cryst.* **36**, 86-95 (2003).
7. Coelho, A. *TOPAS-Academic*, Version 4.1, Coelho Software, Brisbane, **2007**.
8. Newville, M. IFEFFIT: interactive XAFS analysis and FEFF fitting. *J. Synchrotron Rad.* **8**, 322-324 (2001).
9. Rehr, J. J. & Albers, R. C. Theoretical approaches to x-ray absorption fine structure. *Rev. Mod. Phys.* **72**, 621-654 (2000).
10. (a) Kresse, G. & Hafner, J. *Phys. Rev. B* **37**, 558 (1993). (b) Kresse, G. & Hafner, J. *Phys. Rev. B.* **49**, 14251 (1994). (c) Kresse, G. & Furthmüller, J. *Comput. Mat. Sci.* **6**, 15 (1996). (d) Kresse, G. & Furthmüller, J. *Phys. Rev. B.* **54**, 11169 (1996).
11. (a) Perdew, J. P. & Wang, Y. *Phys. Rev. B*. **45**, 13244 (1992). (b) Perdew, J. P., Burke, K. & Ernzerhof, M. *Phys. Rev. Lett*. **77**, 3865 (1996). (c) Perdew, J. P., Ernzerhof, M. & Burke, K. *J. Chem. Phys.* **105**, 9982 (1996).
12. (a) Anisimov, V. I., Zaanen, J. & Andersen, O. K. *Phys. Rev. B.* **44**, 943 (1991). (b) Anisimov, V. I., Solovyev, I. V., Korotin, M. A., Czyzyk, M. T. & Sawatzky, G. A. *Phys. Rev. B.* **48**, 16929 (1993). (c) Solovyev, I. V., Dederichs, P. H. & Anisimov, V. I. *Phys. Rev. B.* **50**, 16861 (1994). (d) Liechtenstein, A. I., Anisimov, V. I. & Zaanen, J. *Phys. Rev. B.* **52**, 5467 (1995). (e) Dudarev, S. L., Botton, G. A., Savrasov, S. Y., Humphreys, C. J. & Sutton, A. P. *Phys. Rev. B.* **57**, 1505 (1998).
13. Verma, P., Xu, X. & Truhlar, D. G. *J. Phys. Chem. C.* **117**, 12648 (2013).

14. (a) Frisch, M. J., Trucks, G. W., Schlegel, H. B., Scuseria, G. E., Robb, M. A., Cheeseman, J. R., Scalmani, G., Barone, V., Mennucci, B., Petersson, G. A., Nakatsuji, H., Caricato, M., Li, X., Hratchian, H. P., Izmaylov, A. F., Bloino, J., Zheng, G., Sonnenberg, J. L., Hada, M., Ehara, M., Toyota, K., Fukuda, R., Hasegawa, J., Ishida, M., Nakajima, T., Honda, Y., Kitao, O., Nakai, H., Vreven, T., Montgomery, Jr., J. A., Peralta, J. E., Ogliaro, F., Bearpark, M., Heyd, J. J., Brothers, E., Kudin, K. N., Staroverov, V. N., Kobayashi, R., Normand, J., Raghavachari, K., Rendell, A., Burant, J. C., Iyengar, S. S., Tomasi, J., Cossi, M., Rega, N., Millam, J. M., Klene, M., Knox, J. E., Cross, J. B., Bakken, V., Adamo, C., Jaramillo, J., Gomperts, R., Stratmann, R. E., Yazyev, O., Austin, A. J., Cammi, R., Pomelli, C., Ochterski, J. W., Martin, R. L., Morokuma, K., Zakrzewski, V. G., Voth, G. A., Salvador, P., Dannenberg, J. J., Dapprich, S., Daniels, A. D., Farkas, Ö., Foresman, J. B., Ortiz, J. V., Cioslowski, J. & Fox, D. J. *Gaussian 09*, Revision A.02, Gaussian, Inc., Wallingford CT, 2009. (b) Zhao, Y., Peverati, R., Yang, K. & Truhlar, D. G. *MN-GFM 6.4*.
15. Zhao, Y. & Truhlar, D. G. *J. Chem. Phys*. **125***,* 194101 (2006).
16. Zhao, Y. & Truhlar, D. G. *Theor. Chem. Acc*. **120**, 215 (2008).
17. Zhao, Y. & Truhlar, D. G. *J. Chem. Theory Comput*. **4**, 1849 (2008).
18. Zhao, Y. & Truhlar, D. G. *J. Phys. Chem. A* **108**, 6908 (2004).
19. Zhao, Y. & Truhlar, D. G. *J. Phys. Chem. A* **109**, 5656 (2005).
20. Hehre, W. J., Radom, L., Schleyer, P. v. R. & Pople, J. A. Ab Initio Molecular Orbital Theory, Wiley, New York, 1986.
21. (a) Dolg, M., Wedig, U., Stoll, H. & Preuss, H. *J. Chem. Phys*., **86**, 866 (1987). (b) Martin, J. M. L. & Sundermann, A. *J. Chem. Phys*., **114**, 3408 (2001).
22. Hehre, W. J., Radom, L., Schleyer, P. v. R. & Pople, J. A. Ab Initio Molecular Orbital Theory, Wiley, New York, 1986.
23. Ertem, M. Z., Gagliardi, L. & Cramer, C. J. *Chem. Sci*., **3**, 1293 (2012).
24. Roos, B. O., Taylor, P. R. & Siegbahn, P. E. M. *Chem. Phys*. **48**, 157 (1980).
25. (a) Andersson, K., Malmqvist, P.-Å. & Roos, B. O. *J. Chem. Phys*. **96**, 1218 (1992). (b) Andersson, K., Malmqvist, P. A., Roos, B. O., Sadlej, A. J. & Wolinski, K. *J. Phys. Chem*. **94**, 5483 (1990).
26. Aquilante, F., De Vico, L., Ferre, N., Ghigo, G., Malmqvist, P.-Å., Pedersen, T., Pitonak, M., Reiher, M., Roos, B. O., Serrano-Andreś, L., Urban, M., Veryazov, V. & Lindh, R. *J. Comput. Chem*. **31**, 224 (2010).
27. (a) Douglas, M. & Kroll, N. M. *Ann. Phys.* **1974**, *82*, 89 (1974). (b) Hess, B. A. *Phys. Rev. A* **33**, 3742 (1986).
28. (a) Aquilante, F., Pedersen, T. B. & Lindh, R. *J. Chem. Phys*. **126**, 194106 (2007). (b) Aquilante, F., Pedersen, T. B., Lindh, R., Roos, B. O., De Meras, A. S. & Koch, H. *J. Chem. Phys*. **129**, 24113 (2008). (c) Aquilante, F., Malmqvist, P.-A., Pedersen, T. B., Ghosh, A. & Roos, B. O. *J. Chem. Theory Comp*. **4**, 694 (2008).
29. (a) Roos, B. O., Lindh, R., Malmqvist, P. A., Veryazov, V. & Widmark, P. O. *J. Phys. Chem. A* **108**, 2851 (2004). (b) Roos, B. O., Lindh, R., Malmqvist, P. A., Veryazov, V. & Widmark, P. O. *J. Phys. Chem. A* **109**, 6575 (2005).
30. Lee, P. A., Citrin, P. H., Eisenberger, P. & Kincaid & B. M. *Rev. Mod. Phys.* **53**, 769-806 (1981).

31. Queen, W. L., Brown, C. M., Britt, D. K., Zajdel, P., Hudson, M. R. & Yaghi, O. M. *J. Phys. Chem. C.* **115**, 24915-24919 (2011).
32. Tishchenko, O., Zheng, J. & Truhlar, D. G. *J. Chem. Theory Comput.* **4**, 1208 (2008).